IOP Publishing Metrologia

Metrologia **57** (2020) 055005 (23pp) https://doi.org/10.1088/1681-7575/ab948b

Qualification and frequency accuracy of the space-based primary frequency standard PHARAO

Ph Laurent[1], F X Esnaut[2], K Gibble[3], P Peterman[3], T Lévèque[2], Ch Delaroche[2], O Grosjean[2], I Moric[1], M Abgrall[1], D Massonnet[2] and Ch Salomon[4]

[1] SYRTE, Observatoire de Paris, PSL Research University, CNRS, Sorbonne Université, UPMC Université Paris 06, LNE, 61 avenue de l'Observatoire, 75014, Paris, France
[2] Centre National d'Etudes Spatiales, 18 avenue Edouard Belin, 31400, Toulouse, France
[3] Department of Physics, The Pennsylvania State University, University Park, PA 16802, United States of America
[4] Laboratoire Kastler Brossel, ENS-PSL Research University, CNRS, UPMC, Sorbonne Université, Collège de France, 24 rue Lhomond, 75005, Paris, France

E-mail: philippe.laurent@obspm.fr

Received 6 February 2020, revised 30 April 2020
Accepted for publication 19 May 2020
Published 30 September 2020

Abstract

The flight model of the laser-cooled cesium atomic clock, PHARAO, has been qualified for operation in space. The clock has passed the vibration, thermal and electromagnetic compatibility tests required to fly in low Earth orbit (400 km). On the ground, the clock realized a typical frequency stability of $3.0 \times 10^{-13}\ \tau^{-1/2}$ with an estimated accuracy of 2.3×10^{-15}. Frequency comparisons with the SYRTE primary frequency standard FOM agree within their stated accuracies. Because PHARAO is optimized for the longer interaction times possible in microgravity, we expect a frequency stability of $1.1 \times 10^{-13}\ \tau^{-1/2}$ and a frequency accuracy of 1.1×10^{-16} for operation in space. The clock has been delivered to the European Space Agency for the assembly of the ACES payload and is scheduled to be launched into space in 2021.

Keywords: cold atom clock, fundamental physic in space, PHARAO, ACES

(Some figures may appear in colour only in the online journal)

1. Introduction

Clocks in space are centerpieces of numerous applications in navigation (GNSS), Earth, ocean and atmosphere monitoring, geodesy and in fundamental physics, for instance relativity tests and space Very Large Baseline Interferometry (VLBI). Primary frequency standards in space add the capability to bring accuracy in time comparisons and positioning. One can foresee a future where Primary Frequency Standards in space and advanced time transfer systems, microwave or optical, realize precise and independent space-time reference frames that are highly immune to the variations of the gravitational potential on Earth.

The development of atomic clocks for space applications is part of a general trend to take advantage of the high degree of control of atoms that laser cooling and trapping provides. Laser cooling routinely delivers atoms at microKelvin temperatures, corresponding to rms speeds of 7 mm s^{-1} for cesium (Cs) atoms [1], and evaporative cooling yields even lower temperatures, of the order of 100 picoKelvin, including Bose–Einstein condensed samples (BEC) [2]. At these temperatures, the Earth's gravitational potential is significant, even for trapped atomic gases [3]. The microgravity environment in orbiting satellites removes this perturbation and allows even lower temperatures, for example, via delta kick cooling [4]. Microgravity also enables much longer free precession times T. The sensitivity of atomic clocks improves proportional to T, and T^2 for matter-wave interferometers [5]. Such instruments in space open new possibilities for precision measurements in various domains, including time and frequency

metrology, geodesy and potentially gravitational wave detection [6].

Cold atom experiments in microgravity have progressed rapidly, using parabolic flights of airplanes [7–9], drop-towers [10], sounding rockets [11] and orbiting satellites. On satellites, a rubidium BEC has recently been produced onboard the International Space Station (ISS) [12] and a laser-cooled rubidium clock operated for more than a year on a Chinese satellite, demonstrating a resonance linewidth similar to ground-based atomic fountains [13]. With high-performance time and frequency links, ACES and other cold-atom satellite clocks will enable comparisons between orbiting and terrestrial clocks, and between clocks distributed around the Earth, that exceed the current state-of-the-art [14].

Here, we present the qualification of the PHARAO (Projet d'Horloge Atomique par Refroidissement d'Atomes en Orbite) space clock. Its goals include operating a laser-cooled Cs clock in space as a primary frequency standard and testing fundamental physics. This project is supported by the French Space Agency, CNES. The first experiments were conducted in 1997 with the test of a clock prototype in the absence of gravity during parabolic flights of a jet airplane [8]. In 1998, the ACES mission, Atomic Clock Ensemble in Space, was accepted by the European Space Agency (ESA), with PHARAO as a central instrument. ACES [15–17] is scheduled to fly onboard the ISS mid 2021. The payload will be attached to an external facility of the Columbus module. In addition to demonstrating a high-performance primary frequency standard in space, the ACES mission is dedicated to fundamental physics tests, a high precision gravitational redshift measurement and a search for a time or spatial variation of fundamental physical constants. For the redshift test, a stable timescale realized from the ACES instruments orbiting in a nearly circular orbit at an altitude of 400 km, provides the proper time of Cs atoms in a freely falling reference frame. Comparing this ACES timescale with ground-based timescales, also based on primary Cs standards, and using a high-performance time transfer system, will test the gravitational redshift at 2.0×10^{-6} [17]. This will represent a factor 70 improvement over the Gravity probe A space mission [18] and a factor ten over the recent test made with two GALILEO satellites in eccentric orbits [19, 20]. In addition, the ACES mission will provide intercontinental frequency comparisons between microwave or optical clocks at the 10^{-17} frequency stability level, complementing the fiber frequency transfer networks developed on continental scale [21, 22].

This paper presents ground test results and analysis of the flight model of the clock to validate its operation in space. The paper is divided in four sections. The next describes the PHARAO clock and its sub-systems, the Cs tube where the atoms are manipulated, the laser source, which provides the laser beams to cool, launch, select and detect the atoms, the microwave source, which provides the 9.2 GHz signals to excite the Cs hyperfine transition, and the computer, which controls the clock operation. This section ends with the environmental tests used to qualify these systems and a description of the software models used to evaluate and validate PHARAO's performance. The third section presents the frequency stability measured during the ground tests and its extrapolation to microgravity operation. Section 4 details the systematic effects that shift the clock's frequency. Here, a significant component is the analysis of the potential residual Doppler shifts. Finally, we summarize the accuracy budget and discuss a mission scenario that allows the systematic shifts to be evaluated at a frequency inaccuracy of 1.1×10^{-16} in space.

2. The PHARAO instrument

PHARAO uses laser-cooled Cs atoms, directly captured from a vapor with optical molasses [23]. The cold atoms are launched along the symmetry axis of the vacuum chamber (see figure 1) with an adjustable velocity. In a clock cycle, atoms are first prepared in the $F = 4$ ground state, the atoms in $m_F = 0$ are then transferred to $F = 3$, $m_F = 0$ in the preparation cavity, the atoms remaining in $F = 4$ are cleared. The atoms in state 3 and 0 are interrogated by the 9.2 GHz microwave field, and finally detected via laser fluorescence.

2.1. The PHARAO sub-systems

The vacuum chamber of the Cs tube is shown in figure 1. A Cs reservoir provides the capture zone with a low Cs vapor pressure. A motorized valve and the regulated temperature of the reservoir control the flux of the vapor. Typically, the Cs pressure is 2×10^{-6} Pa in the capture zone. The residual vacuum, 2×10^{-8} Pa, is maintained by a 2 l s^{-1} ion pump and five getters, and is monitored via the ion pump current.

The laser source is described in [24]. It delivers light on ten optical fibers to the Cs tube, six for the optical molasses beams, two for the selection beams and two for the detection beams. All the fiber output powers are measured by photodiodes inside the Cs tube and analog servo loops stabilize the power of each pair of counter-propagating cooling beams and the detection beams. The six cooling laser beams are collimated with a waist radius of 5.25 mm and have a maximum power of 12 mW per beam. The laser source has a mass of 21 kg, a volume of 35 l and a power consumption of 35 W.

At the beginning of a clock cycle, atoms are loaded into optical molasses, which is monitored by a photodiode detecting the radiated fluorescence. The atoms are launched in the upper hyperfine level ($6s_{1/2}$, $F = 4$) into the cylindrical TE_{011} preparation cavity after passing through a graphite ring to getter Cs vapor. The cavity has a 37 mm long cut-off waveguide at its entrance and a 31 mm long waveguide cut-off at its exit. The cavity field transfers atoms to the lower hyperfine level ($6S_{1/2}$ $F = 3$) in a well-defined Zeeman state, $m_F = 0$ for clock operation or $m_F = 1$ for magnetic field measurement. The Zeeman sub-levels are split by a static magnetic field from a coil surrounding the cavity, typically 0.5 μT at the center of the preparation cavity. The field decreases slowly (0.1 μT cm^{-1}) to a homogeneous bias field of 0.1 μT in the Ramsey interrogation zone.

After the preparation cavity, the atoms in the upper level $6S_{1/2}$ $F = 4$ are cleared with radiation pressure from the selection laser, tuned to the $6S_{1/2}$, $F = 4 \rightarrow 6P_{3/2}$, $F' = 5$

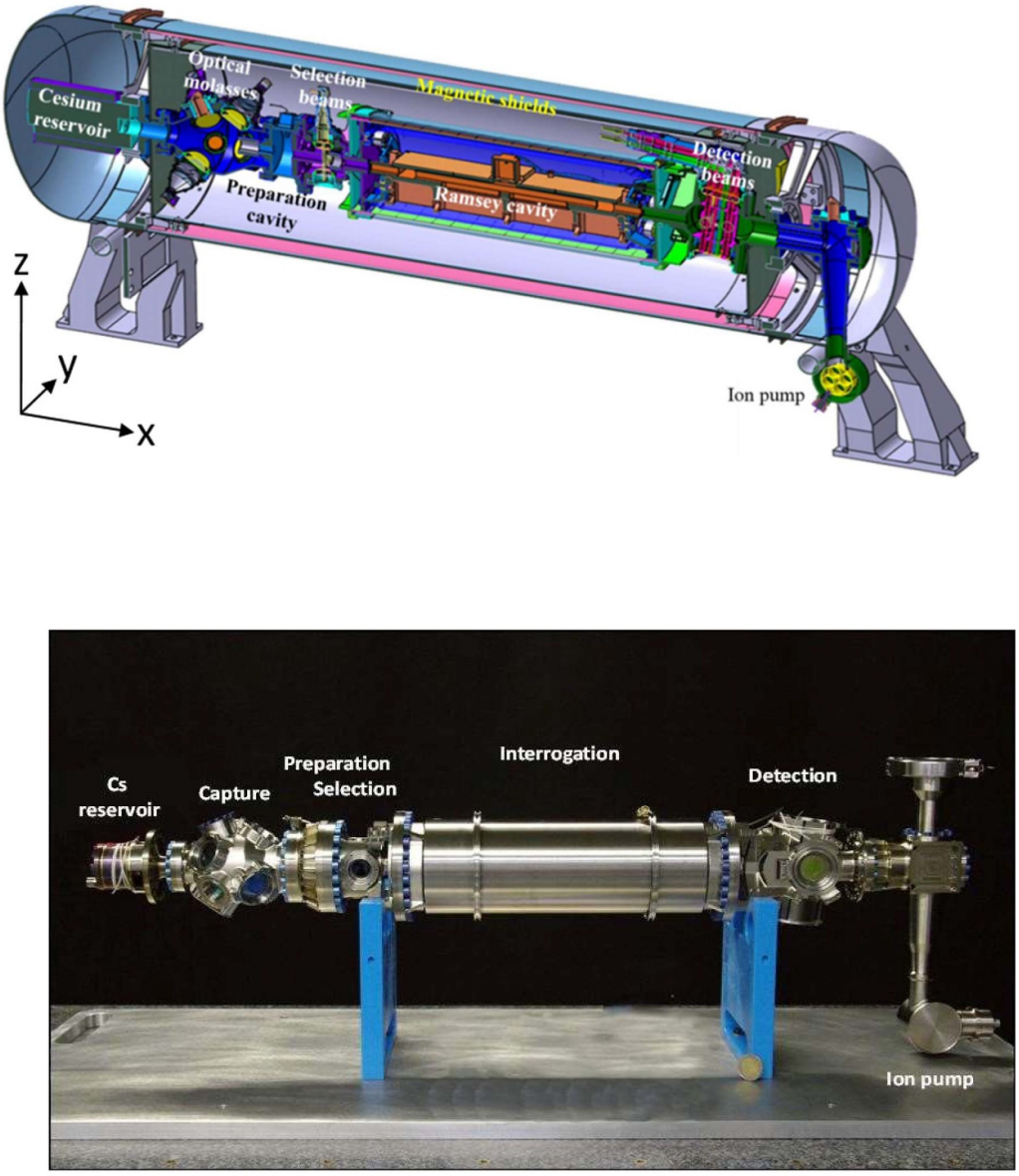

Figure 1. Sketch of the PHARAO Cs tube and photograph of the titanium vacuum chamber. Chamber is surrounded by three magnetic shields and seven coils to produce a stable homogeneous magnetic bias field. Optical fibers deliver the laser light to the chamber and the collimators are fitted with RF filters. The optical molasses region is on the left and atoms are launched towards the detection zone on the right, with an adjustable mean velocity between 0.0492–5 m s^{-1} and a temperature of 1 μK. Desired quantum states are prepared in the microwave preparation cavity and unwanted state populations are cleared by the selection laser beams. Subsequently, the cold atoms experience the two Ramsey interactions and finally the atom number in each hyperfine state is detected by laser-induced fluorescence. Various parts are connected using flexible gaskets that withstand thermal and mechanical stress from thermal cycling and vibration. Vacuum chamber is 910 mm long, has a mass of 45 kg, and consumes 7 W.

cycling which is mul transition. An additional upstream laser beam, tuned to the $6S_{1/2}$, $F = 3 \rightarrow 6P_{3/2}$, $F' = 4$ transition, can be pulsed to selectively pump atoms to the upper level ($6S_{1/2}$, $F = 4$) before the pushing beam. The combination of both beams thus can select a narrow, millimeter wide, axial slice of the molasses cloud. This slicing will be useful to reduce the cloud spread in microgravity at low launch velocities and to analyze the atomic velocity distribution.

The state-prepared atoms then enter the copper-ring Ramsey cavity. It has two 19 mm long interaction zones, which are separated by 200 mm. Each zone has two 30 mm long cut-off waveguide sections and the ends of the cavity have 7.6 × 8.6 mm diaphragms, to avoid atomic interaction with the cavity walls. To reduce the cavity's susceptibility to vibrational deformation, the cavity is mounted on a rigid bed made of AlSiC, where its thermal expansion coefficient was matched to pure copper's by varying the SiC concentration. To avoid unintended current loops, the bed is secured to the vacuum chamber with electrical isolation. Microwaves are supplied by a 120 cm long SiO_2 coaxial cable, with a stability of 20fs/°C. The coaxial cable jacket is welded to the vacuum chamber, which ensures the cavity ground. The cable feeds a single

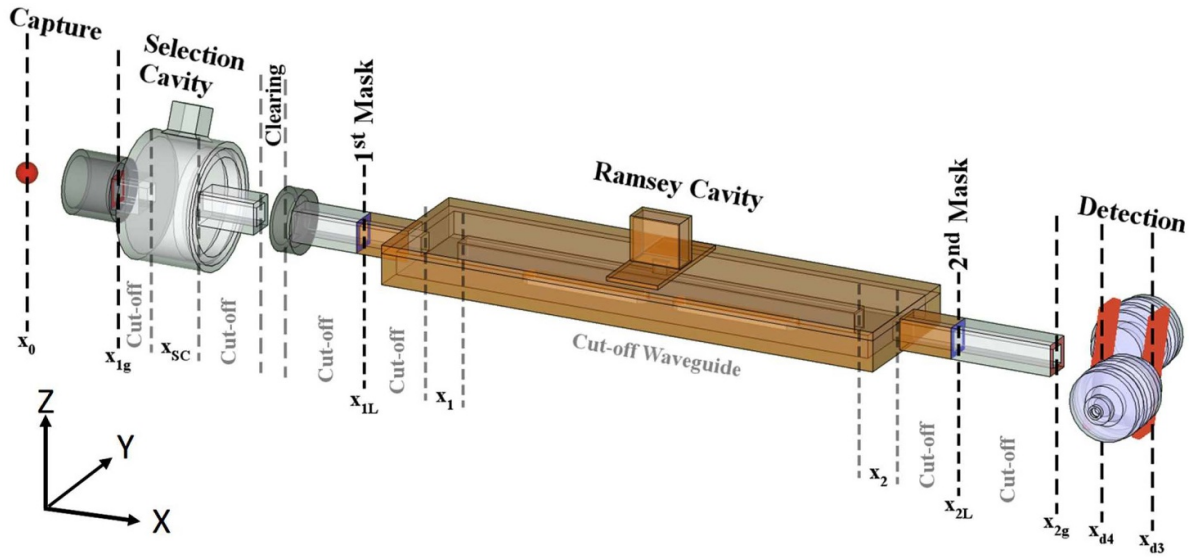

Figure 2. Sketch of the PHARAO selection and Ramsey cavities. Atoms are launched in the x direction, passing through the selection and Ramsey cavities to the detection region. Below cut-off waveguide sections are 8 × 9 mm and the masks are 8.6 × 7.6 mm, with 1 mm radius corners (from [25]).

antenna in a waveguide, and it feeds, through a slit, both sides of the ring cavity, halfway between the interaction zones. The cavity Q is 1000 and the frequency resonance is 3 MHz below the atomic resonance at 9.192 631 770 GHz at the operating temperature of 25 °C. The temperature of the cavity is measured by two calibrated probes. The probes are fixed on the outer walls of the interrogation section of the vacuum chamber, to avoid possible electromagnetic perturbations of the atoms. These are used by the computer to stabilize the temperature of the cavity by means of two external heaters.

A solenoid around the interrogation chamber and two independent end coils provide a DC magnetic bias field. A first cylindrical magnetic shield, with endcaps, encloses this assembly. The vacuum chamber heaters are outside the shield and two additional trim coils surround the shield apertures to ensure magnetic field homogeneity. Two longitudinal wires run parallel to the atoms, inside the inner-most shield and outside the vacuum chamber. One wire is used to demagnetize the inner two shields and the other to drive RF $\Delta m_F = 1$ Zeeman transitions to map the magnetic field along the path of the atoms.

After the Ramsey interrogation, the atoms reach the detection zone where they successively cross four laser beams. The first is a σ^+ polarized standing wave, which induces fluorescence from atoms in the upper $6P_{3/2}$ level on the $6S_{1/2,}$ $F = 4$, $m_F = 4$ to $6P_{3/2,}$ $F = 5$, $m_F = 5$ cycling transition. The fluorescence is focused by a lens system onto the first photodiode, giving a signal (N4), proportional to the number of atoms in the $F = 4$ ground state. The second resonant laser beam, a travelling wave, clears these atoms with radiation pressure. The third beam optically pumps atoms from the lower ($F = 3$, $m_F = 0$) state to the upper hyperfine $F = 4$ state. The fourth beam, identical to the first, gives a fluorescence signal (N3), proportional to the number of atoms in the $F = 3$ level, which is recorded by a second lens system and photodiode. Each amplified photodiode is thermally stabilized to 18 °C with a Peltier cooler. Beams 1, 2 and 4 come from a single optical fiber and the total laser power is stabilized by an analog servo acting on an acousto optic modulator (AOM) in the laser source subsystem. The efficiency of the fluorescence collection depends on the distance between the atoms and the photodetector, with a gradient from 9%, for atoms passing close to the lens, to 6% on the axis, to 4% for atoms far from the lens. Because the two photodetectors are on opposite sides of the detected atomic cloud (see figure 2), the opposite gradients of the collection efficiencies in the y direction make the signals N3, N4, and N3 + N4 more sensitive to the transverse position of the atoms than the transition probability, N3/(N3 + N4).

A second cylindrical magnetic shield with end caps surrounds the vacuum chamber from the capture to the detection. A solenoid is wired around the shield and by means of a 1D magnetic probe outside the shield, the computer performs a magnetic field servo loop to stabilize the field inside the outermost magnetic shield [26]. For a ±40 μT external magnetic field variation, this control loop reduces its effect by one order of magnitude beyond the passive shield attenuation. A third magnetic shield encloses the whole chamber, except the ion pump, which is enclosed by a dedicated magnetic shield. The magnetic configuration is detailed in [27] and the global magnetic attenuation factor is 270 000.

All photodiode signals are digitized by the computer and, synchronous with the clock cycle, the computer calculates the populations of each hyperfine level and derives a frequency correction to be sent to the microwave source (figure 3) before the next clock cycle.

The microwave signals at 9.2 GHz are synthesized in two parts. First, a low-phase-noise 5 MHz quartz oscillator with low acceleration sensitivity is frequency multiplied and mixed with a direct digital synthesis (DDS) to provide a tunable 100 MHz signal. The second stage receives the 100 MHz signal (or an external one), which is multiplied

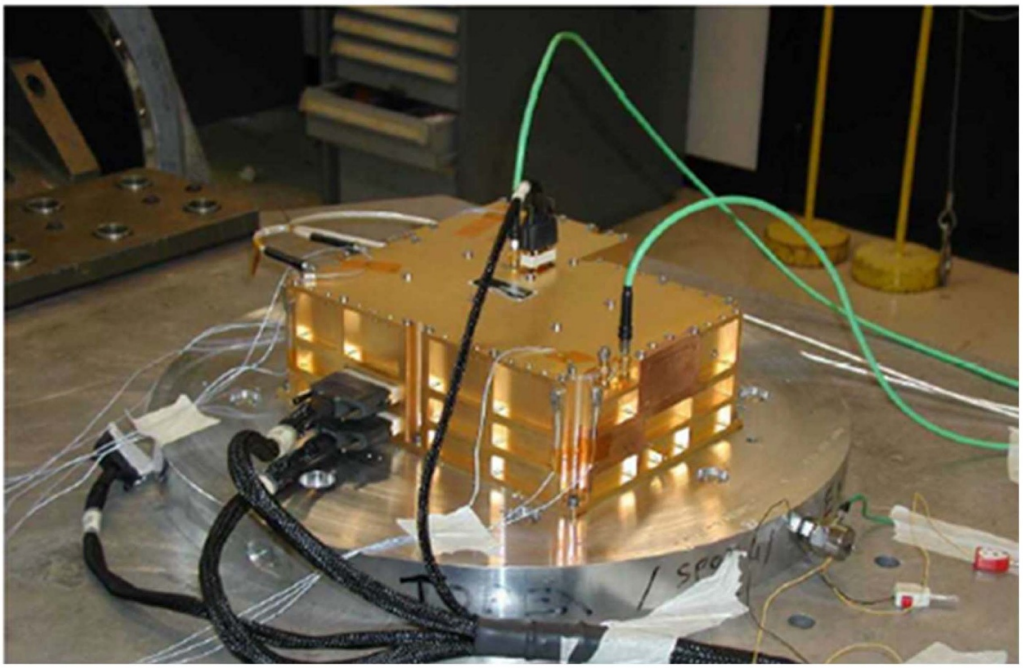

Figure 3. Microwave source under vibration tests. It provides tunable signals at 100 MHz and 9.2 GHz, synthesized from a 5 MHz ultra-stable quartz oscillator. Microwave source has a mass of 7 kg, a volume of 8 l and consumes 24 W.

and mixed with a second DDS and then split to provide two tunable 9.2 GHz signals for state preparation and Ramsey interrogation with a frequency resolution of 118 nHz. The outputs can be attenuated by up to 60 dB in 0.02 dB steps. In addition, the microwave power can be switched off, with at least 80 dB of attenuation. During the ground clock operation, the first DDS was the actuator for the phase lock loop to the hydrogen maser. The second DDS modulated the microwave signal and received the clock frequency corrections.

The real-time operation of the clock is orchestrated by the computer, which sends all triggers and parameters to the PHARAO sub-systems and acquires measurements. The computer also arranges telemetry data in two types of packets: housekeeping data, which are measurements performed every 10 s to survey some parameters (temperatures, error signals of the various servo loops for instance), and clock data performed in real time with the clock cycle (laser powers and atomic signals). The computer also initializes the clock and supports several operating modes: hardware health verification, cold atom optimization, clock evaluation and clock operation.

2.2. ACES integration

The clock sub-systems, depicted in figure 4, were assembled on the ACES baseplate at CNES, Toulouse, before being covered by a multilayer insulator. To simulate operation in orbit, the clock was placed in a vacuum chamber (10^{-4} Pa) with the Cs tube aligned vertically and the cold atoms are launched upwards. A computer varies the temperature of the baseplate to simulate thermal fluctuations and drives coils around the vacuum chamber to simulate slow variations of the magnetic field that will be seen by PHARAO in orbit.

For the qualification, the 100 MHz oscillator of PHARAO was phase-locked to an external hydrogen maser (0.5 Hz bandwidth) in the same way, as it will be locked to the ACES SHM. The mobile Cs fountain FOM [28] simultaneously measured the frequency of the hydrogen maser to extract the frequency difference PHARAO-FOM. The PHARAO outputs at 100 MHz and 9.2 GHz can also be mixed with a cryogenic oscillator [29] to analyze noise levels and potential phase transients synchronous with the clock cycle. The 100 MHz PHARAO input can also receive 100 MHz synthesized from the cryogenic oscillator to generate the 9.2 GHz interrogation signal with a low phase noise. The clock is driven and controlled by the ground segment through a serial line: commands are sent to the clock and telemetry packets are received, sorted, visualized and analyzed.

2.3. Environmental tests

To analyze the behavior of the sub-systems, mechanical and structural models have initially been built and equipped with temperature probes and accelerometers. These were subjected to all of the environmental tests, with higher limits than are expected during the mission. These experiments have been supplemented by finite element models whose parameters are fitted to match the experimental results. These models have subsequently been used to test modifications, increase margins and identify improvements. Another model of the clock, the engineering model, has also been built to validate the clock operation [30, 31].

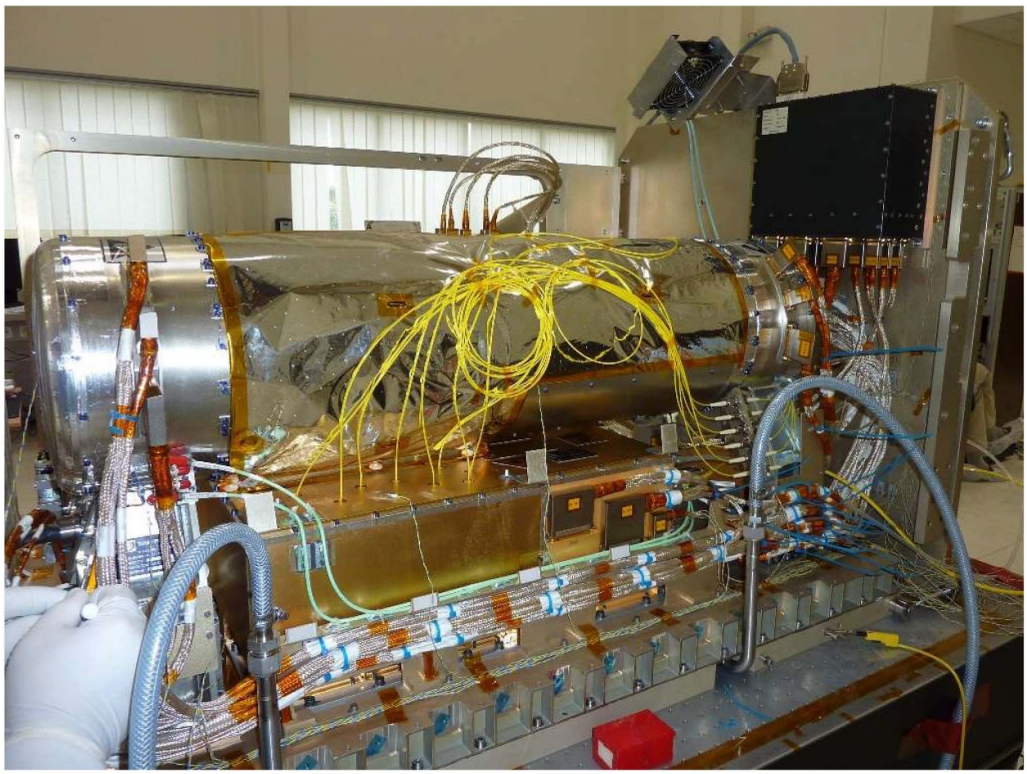

Figure 4. PHARAO flight model integrated on the ACES baseplate. Laser source and the microwave source are underneath the Cs tube. Yellow cables are the optical fibers and the computer is on the right vertical wall. Clock was assembled at CNES, Toulouse.

Thermal models predict baseplate fluctuations of ± 1.5 °C at the orbital period and slower seasonal variations, which are bounded between 10 °C –33 °C. To cope with these fluctuations, several internal temperatures are controlled by the computer with 0.1 Hz bandwidth: the optical bench at 26 °C$\pm$ 0.2 °C, the Cs reservoir at 35 °C $\pm$ 0.2 °C, the detection photodiodes at 18 °C $\pm$ 0.2 °C and the Ramsey interrogation cavity at 25 °C $\pm$ 0.05 °C. The PHARAO storage temperature is between -40 °C and 40 °C and the vacuum chamber was heated to 140 °C during outgassing. A second significant orbital fluctuation is the Earth's magnetic field, which has amplitude of ± 40 μT. Therefore, the microwave source, the Cs saturated absorption cells of the laser source, and, of course, the Cs tube are magnetically shielded.

The vibration levels of the launch vehicle are simulated on a shaker, of 2 min duration with a standard deviation of 80 m s^{-2}, and shocks are simulated with a sinusoidal amplitude of 300 m s^{-2} at 30 Hz for 1 min.

The cumulated radiation dosage onboard the ISS is relatively low, about 13 krads/3 years. Only a few electronic components had to be radiation hardened: the computer and the DDS of the microwave source. Other components have been validated with analysis or radiation tests.

The clock architecture has been finalized using these studies and the flight model has been built. All PHARAO sub-systems were qualified at the environmental levels described above, as well as with electromagnetic compatibility (EMC) tests (sensitivity to external electromagnetic signals: conductive and radiative injected fields in a wide frequency band). These tests were successful and the sub-systems have been delivered for the final assembly of the PHARAO clock and its performance tests, which we describe in the next section.

2.4. Simulations of PHARAO

To analyze the experimental results we developed Monte Carlo simulation software to calculate the evolution of the atoms. The simulations account for the mechanical and optical geometry of the Cs tube. One simulation displays the evolution of the atomic cloud along the Cs tube and calculates the two-state Bloch vector evolution as well as the detected signals. The measured time of flight profiles and number of atoms, as a function of the clock cycle parameters (laser powers, laser frequency, durations of the launch and cooling phases), agree with this model. This software also allows us to define the timetable of a clock cycle for any launch velocity on Earth and in space. Timetables for several launch velocities are preloaded in the flight software and will be used during the commissioning phase of ACES. Additional more specific Monte Carlo simulations are used to evaluate distributed cavity phase (DCP), microwave lensing and cold collision frequency shifts. These, particularly those used to analyze DCP shifts, are extensions of the well-tested simulations that were developed to analyze DCP shifts of fountain clocks [32]. In these, the tipping angle and effective phase [32, 33] are calculated on a

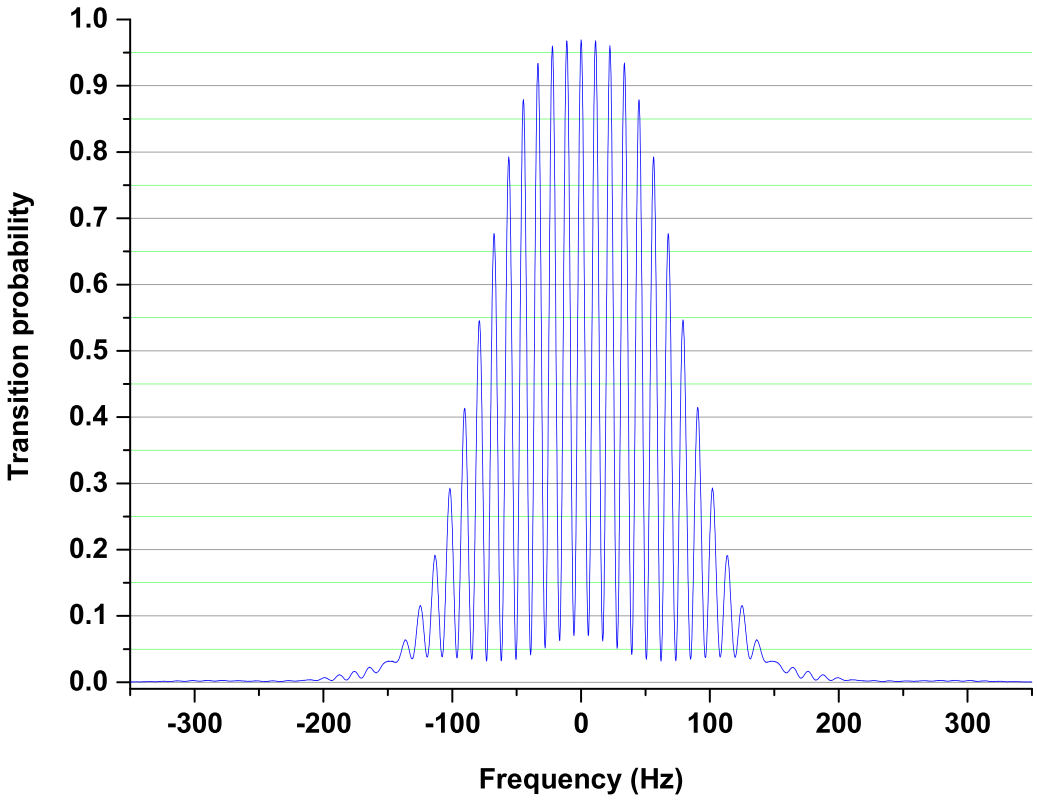

Figure 5. Experimental Ramsey fringes near 9.192 GHz for atoms prepared in the $F = 3$ $m_F = 0$ state. Transition probability is the ratio of the number of atoms detected in $F = 3$ over the total detected atom number.

transverse position grid and then are interpolated for each trajectory, instead of integrating the Bloch evolution for each.

3. Frequency stability

Figure 5 shows the Ramsey fringes for atoms prepared in the $F = 3$ $m_F = 0$ Zeeman state in the state selection cavity. The central fringe is 5.6 Hz wide, the contrast is 0.899, and the signal-to-noise ratio for a single launch is of the order of 1000. The unequal microwave excitations in each Ramsey cavity zone reduce the contrast because gravity decelerates the atoms between the two zones for an upward launch; when the first microwave pulse is $\pi/2$, the second is 1.4 $\pi/2$. With full trapping laser beam intensities, we load 5×10^8 cold atoms in optical molasses (11% are in the $m_F = 0$ sublevel). The short transit time on Earth leads to the detection of too many atoms, causing the fluorescence signals to saturate. We therefore decrease the initial number of atoms to a few times 10^7 by loading for only 200 ms and reducing the laser power to 5 mW per beam, from 12 mW per beam. The atoms are launched upwards at 3.54 m s^{-1}, given by the frequency difference between the three upward and downward propagating laser beams, and they reach the detection region with a velocity of about 1 m s^{-1}. The standard deviation of the nearly Gaussian velocity distribution is 8 mm s^{-1} in each dimension, corresponding to a temperature of 1.0 μK. The Ramsey interrogation time is 90 ms and the duration of this clock cycle is 590 ms.

During clock operation, the microwave frequency is slowly modulated, normally by 2.8 Hz on the ground, to probe each side of the central resonance and derive the frequency corrections. The corrections are sent to a DDS of the microwave source.

Figure 6 shows the frequency stability of the comparison of the SYRTE FOM fountain and PHARAO. During this long duration, recording PHARAO is exposed to the simulated orbital environment, ±1.5 °C variations of the baseplate temperature and ±40 μT magnetic field variations with a period of 5400 s. PHARAO's contribution to the measured Allan deviation is 3.0×10^{-13} $\tau^{-1/2}$. It is limited by the resonance width of 5.6 Hz, combined with the quartz oscillator instability of 9×10^{-14} at 1 s, via aliasing noise, the Dick effect [34]. The narrower FOM linewidth of 1.2 Hz yields a higher stability of 1.4×10^{-13} $\tau^{-1/2}$. The frequency stability of the comparison reaches 1.8×10^{-15} after 40 000 s of averaging.

The noise sources of PHARAO have been analyzed by operating the clock in two configurations: the nominal one uses the internal quartz oscillator, and the second mode uses an external cryogenic oscillator to directly feed the 100 MHz input of the microwave source. In the latter case, the noise contributed by the microwave source is negligible (10^{-14}@1 s). We measure the frequency stability as the number of atoms N is varied over two orders of magnitude and observe an $N^{-1/2}$ dependence, as expected for quantum projection noise [35] (laser noise and detection noise are negligible [24]). By comparing the two configurations,

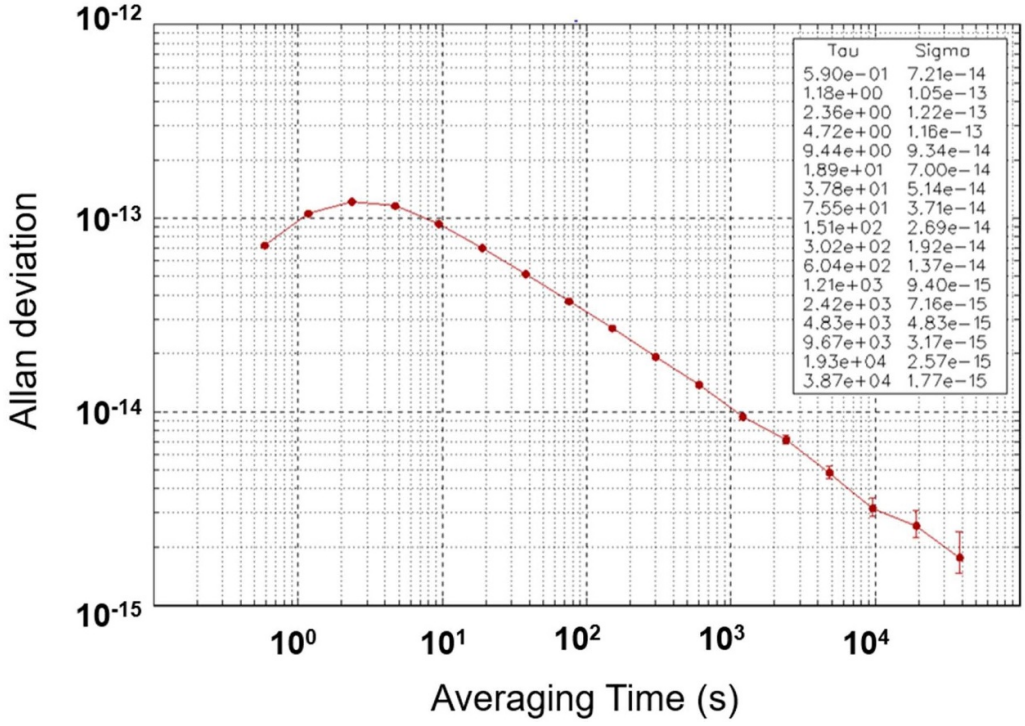

Figure 6. Allan deviation of the frequency difference of PHARAO and FOM, demonstrating an instability of $3.3 \times 10^{-13}\ \tau^{-1/2}$. During these measurements, PHARAO was exposed to simulated thermal and magnetic orbital fluctuations.

the frequency noise contributed by the microwave source is $2.6 \times 10^{-13}\ \tau^{-1/2}$, which is consistent with the calculated contribution using the measured phase noise spectrum of the 9.2 GHz signal and the sensitivity function [34].

In microgravity, the number of atoms prepared in $m_F = 0$ is estimated to be $5 \times 10^7 \times (1-\exp(-t/0.5))$, where t is the loading time in seconds. Figure 7 shows the calculated frequency instability for different launch velocities with an optimized loading time for each. The lowest frequency instability, $1.05 \times 10^{-13}\ \tau^{-1/2}$, is expected for launch velocities of 300–400 mm s^{-1}. Contributions to the instability include the quantum projection noise, which dominates for low atom numbers at small velocities, and the quartz oscillator noise via the Dick effect, which dominates for large Ramsey resonance linewidths at high launch velocities.

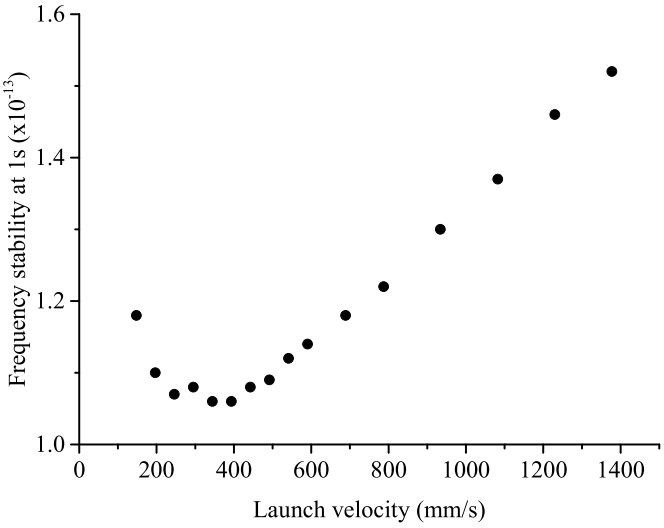

Figure 7. Predicted frequency instability at 1 s of PHARAO in microgravity. Instability is minimized for launch velocities of 300–400 mm s^{-1}. This prediction includes the contribution from the measured phase noise of the microwave source, detection noise, quantum projection noise and the molasses loading time. At $v = 300$ mm s^{-1}, the calculated noise slightly increases due to a larger contribution of the microwave source phase noise via the Dick effect.

4. Frequency accuracy

In this section, we examine important systematic effects that can shift the apparent hyperfine transition frequency. Many of these systematic shifts have been studied during ground operation, with an accuracy goal on Earth near 10^{-15}. Because the trajectories of the atoms are different in microgravity, many systematic shifts change significantly, notably the cold collision shift, the DCP shifts and the microwave lensing shift. A 10^{-15} accuracy on Earth combined with simulations of the clock in microgravity show that a frequency accuracy of 10^{-16} is attainable in space.

4.1. Second-order Zeeman shift

The $F = 3\ m_F = 0$ to $F = 4\ m_F = 0$ clock transition frequency has no linear Zeeman shift and varies quadratically with the magnetic field to lowest order. On Earth, a field of

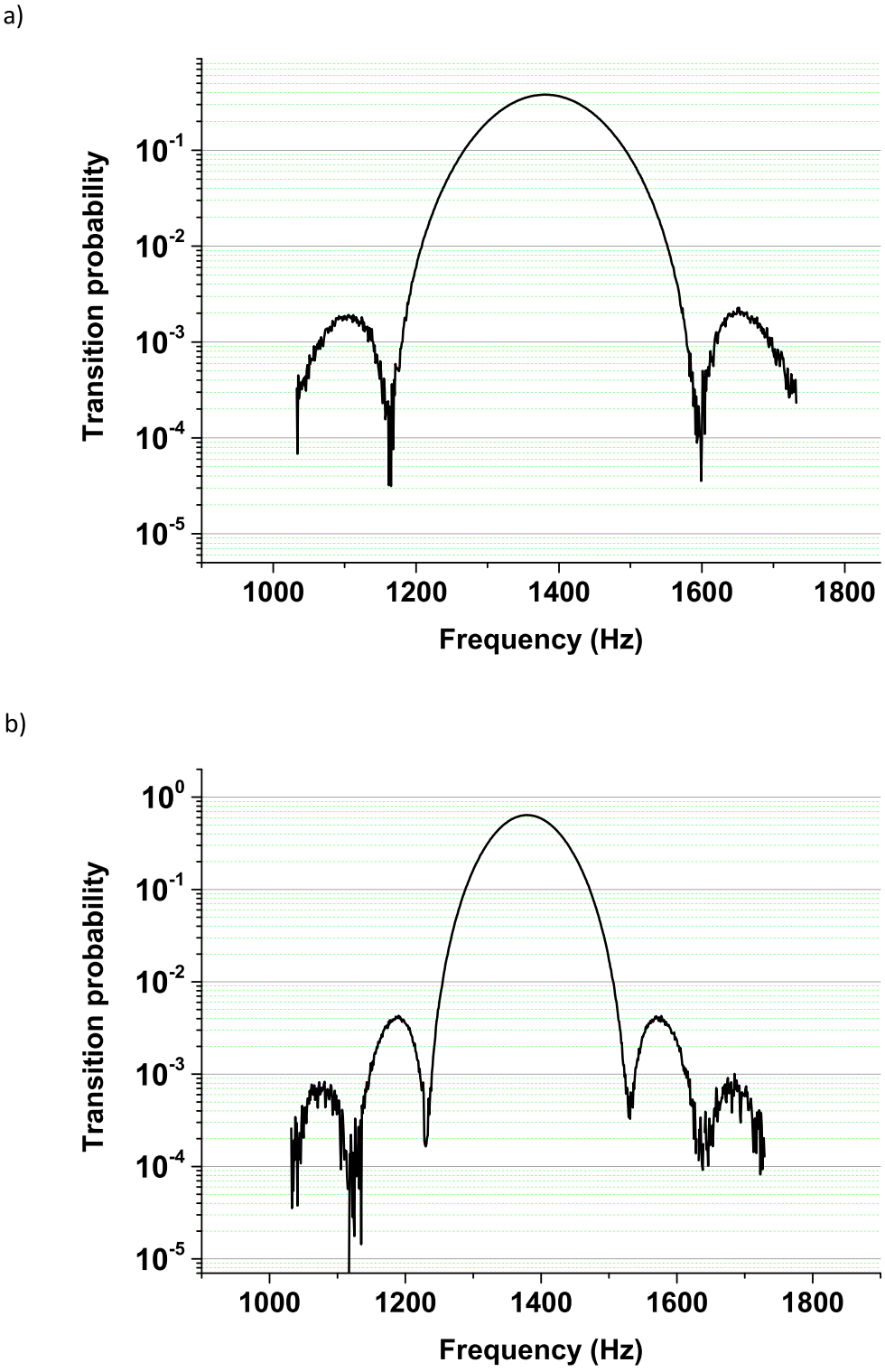

Figure 8. Rabi resonance in the first (a) and second (b) Ramsey interaction zone at optimal Ramsey fringe contrast. Different transition probabilities come from the atom deceleration between the two zones.

0.2 μT is applied in the Ramsey cavity region to separate the adjacent m_F transitions. To measure the magnetic field, we use the field-sensitive resonance between $m_F = 1$ states. Figure 8 shows microwave transitions between $m_F = 1$ states in each interaction zone. The central frequencies are 1380.36 and 1379.62 Hz, and correspond to the mean bias field, which has small local deviations. The high symmetry of the resonances demonstrates the homogeneity of the magnetic field in both interaction zones, resolving the previously observed anomaly in the engineering model of PHARAO from a local magnetization of the magnetic shield end cap [30]. The widths at half maximum of the measured and calculated resonances

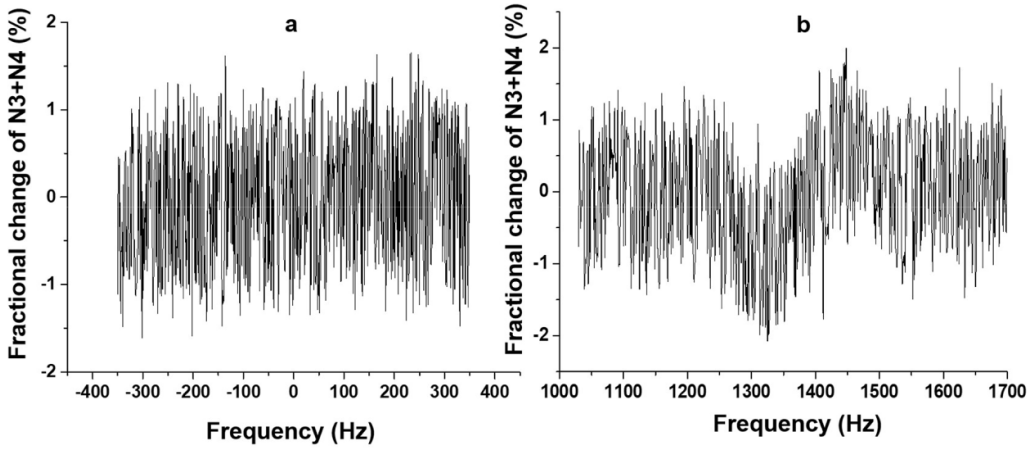

Figure 9. Fractional change of the sum of the two detected fluorescence signals N3 + N4 at optimal power for the second Ramsey interrogation zone, as in figure 8(b). (a) Atoms selected in the F = 3, $m_F = 0$ Zeeman state display no frequency dependence. (b) Atoms selected in the F = 3, $m_F = 1$ Zeeman state show a ± 1%, variation around the resonance at 1383 Hz due to a small magnetic field gradient in the transverse y direction, of the order of 14 pT mm^{-1}.

differ by 1.5 Hz, suggesting a residual magnetic field inhomogeneity of approximately 200 pT over the cloud size.

An interesting signature of a small magnetic field inhomogeneity is observed when the atoms are detected with the two photodetectors. In figure 9 we plot the change of the sum of the detected signals, N3 + N4, versus microwave frequency at the optimal power for the second Ramsey zone (figure 8(b)). For the $m_F = 0$ resonance, no frequency dependence is observed, but, for $m_F = 1$, we see a small variation, ±1%, near the resonance. This is due to a transverse variation of the resonant frequencies of the atoms and the opposite gradients of the collection efficiency in the y direction for the N4 and N3 detectors. Using the measured detection sensitivity variation, we extract a mean transverse magnetic field gradient of 14 pT mm^{-1}. This low field inhomogeneity does not significantly affect the clock accuracy.

We now turn to the mapping of the magnetic field in the Ramsey interaction cavity. The central $m_F = -1$ Ramsey fringe gives the mean magnetic field throughout the Ramsey interrogation region. Figure 10 shows the measured Ramsey fringes. The pattern is symmetric about the central frequency of −1383.1 Hz and the contrast of the central fringe is within 2% of that of the $m_F = 0$ resonance. This reduction corresponds to a linear gradient that has a 14 pT difference across the cloud, consistent with the above measurements.

To assess the quadratic Zeeman shift, we measure the local magnetic field during the atom's free flight between the Ramsey interaction zones, using a 10 ms pulse of oscillating current to the longitudinal wire. We use a typical current of 12 mA and vary the pulse delay to map the field versus position. The amplitude of the radiated magnetic field is attenuated by the copper Ramsey cavity and the attenuation varies along the cavity, by a factor of 10 from the sides to the center, at the operating current frequency (~700 Hz). Figure 11 shows the static magnetic field deduced from the atomic resonance measurements. The accuracy of the map is fractionally 2×10^{-3}. The 2 nT field variation near the center of the cavity is generated by the brazed joint of the antenna of the Ramsey cavity, which was previously observed with a magnetic probe during the characterization of the cavity.

From this map, the calculated F = 3, $m_F = -1$ to F = 4, $m_F = -1$ frequency resonance is detuned by 1381.62 Hz, which is −1.5 Hz lower than the measurement, but within the uncertainty of the map. The calculated contribution of the field inhomogeneity to the quadratic shift, $0.047 \times \left(B^2 - \langle B \rangle^2\right)$, is -2×10^{-8} Hz, which is negligible. Therefore, the mean B field accurately determines the quadratic Zeeman shift. For the F = 3, $m_F = +1$ to F = 4, $m_F = +1$ resonance frequency of 1383.1 Hz, the mean B field gives a clock shift of 1.6648×10^{-3} Hz and we assign a conservative fractional frequency uncertainty of 1×10^{-17}.

The lower launch velocity in microgravity further enables a more accurate magnetic field mapping with better position resolution, since we can thinly slice the atomic cloud in the state preparation region. However, the Earth's magnetic field varies throughout the orbit. During our tests with simulated field variation, we measured a frequency modulation of 0.75 Hz on the $m_F = 1$ resonance, which corresponds to a 10^{-16} modulation of the clock frequency. Although the frequency shift averaged over an orbit is less, the clock frequency seen at any ground station can have a systematic offset. We have also measured a small frequency sensitivity to the temperature of the baseplate for the coil current supplies (10pT°C^{-1}), the offset of the magnetic field probe (30pT°C^{-1}) used by a servo loop to attenuate the magnetic variations, and of a thermally-induced current around the Cs tube (10 pT°C^{-1}). To measure these magnetic field fluctuations, the clock configuration is switched every 500 s to monitor the $m_F = 1$ resonance frequency for 10 s. This determines the residual magnetic field variation and will be used to correct the clock frequency as a function of the ISS position frequency.

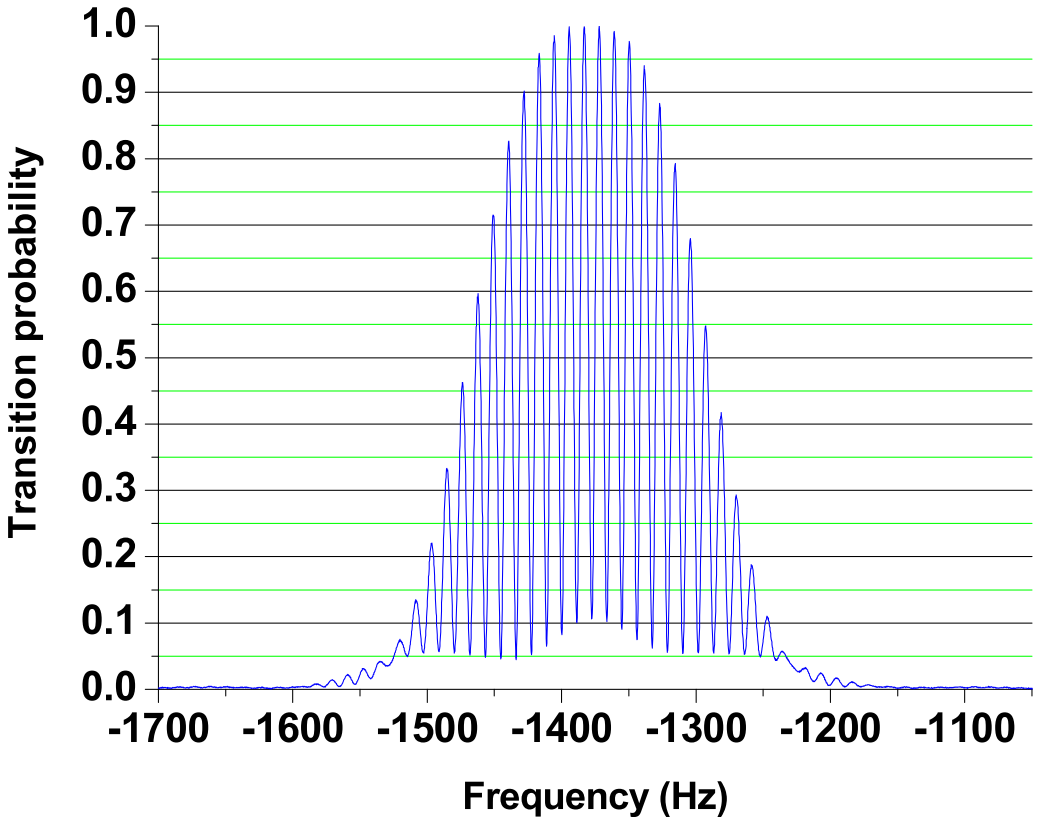

Figure 10. $F = 3$, $m_F = -1$ to $F = 4$, $m_F = -1$ Ramsey resonance.

4.2. Blackbody radiation (BBR) shift

BBR from the environment also shifts the clock transition frequency. Almost the entire shift, 98%, is from radiation from the Ramsey cavity walls, and the remaining is from the cut-off waveguides of the Ramsey cavity. Two calibrated probes placed on the vacuum chamber surrounding the microwave cavity determine the temperature of the cavity. The computer reads these values and actuates two heaters to stabilize the temperatures of the probes. The temperature uncertainty of the probes, including calibration, self-heating, cables, connectors, electronic, digitalization, and aging, is estimated to be $\sigma_p = 33$ mK for each probe.

A second uncertainty contribution to the BBR shift is the temperature difference between the probes and the cavity. We have measured the temperature dependence of the resonance frequency of the copper Ramsey cavity. We use a network analyzer and test the correlation with the probe temperature for four baseplate temperatures, 17 °C, 23 °C, 27.5 °C and 29,5 °C, with and without 1.5 °C modulation, and cavity temperatures over a range of 15 °C to around 25 °C. During these measurements, the Cs tube is under vacuum and we record the temperatures for several hours, which is required to reach steady state. The noise of the measurement of the cavity resonance is 2 kHz. The potential frequency shifts due to the temperature dependence of the cables and connectors has been evaluated to be several kHz and are removed from the measurements. The resonance frequency varies linearly with temperature with a slope of -155.8 kHz °C^{-1} (figure 12(a)). After removing the linear dependence, the residuals do not show a systematic deviation that would suggest a temperature gradient between the cavity and the probes. The residuals have a σ_g of 30 mK (see figure 12(b)).

In addition, we have performed thermal finite element simulations of the Cs tube, including the emissivity and conductivity of all the elements of the tube. The model shows that the temperature difference between the cavity and probes remains below 50 mK for the operating baseplate temperature range of 10 °C–33 °C and cavity stabilization temperatures of 20 °C, 25 °Cand 30 °C, consistent with the above results.

Finally, we estimate the small contribution of the external thermal radiation from the cavity apertures. We use the maximum reflectivity of titanium (0.92) and copper (0.98) along with the Clausing factor for a cylindrical pipe, to describe the radiation diffusion in the cut-offs. This gives external thermal flux contributions of 0.7% for the capture end and 0.5% for the detection end.[1]

In the thermal finite element model, at a baseplate at the nominal temperature of 20 °C and the cavity regulated at 25 °C, the temperature of the capture zone is on average $T_{capt} = 25$ °C with an inhomogeneity of ±1.5 °C. Similarly, the temperature of the detection zone is on average $T_{det} = 23$ °C with an inhomogeneity of ±1.5 °C.

[1] If we neglect reflections inside the cut-off, considering only the solid angle gives contributions of 0.035% and 0.025%, respectively, which are much smaller than the contributions of the external parts above.

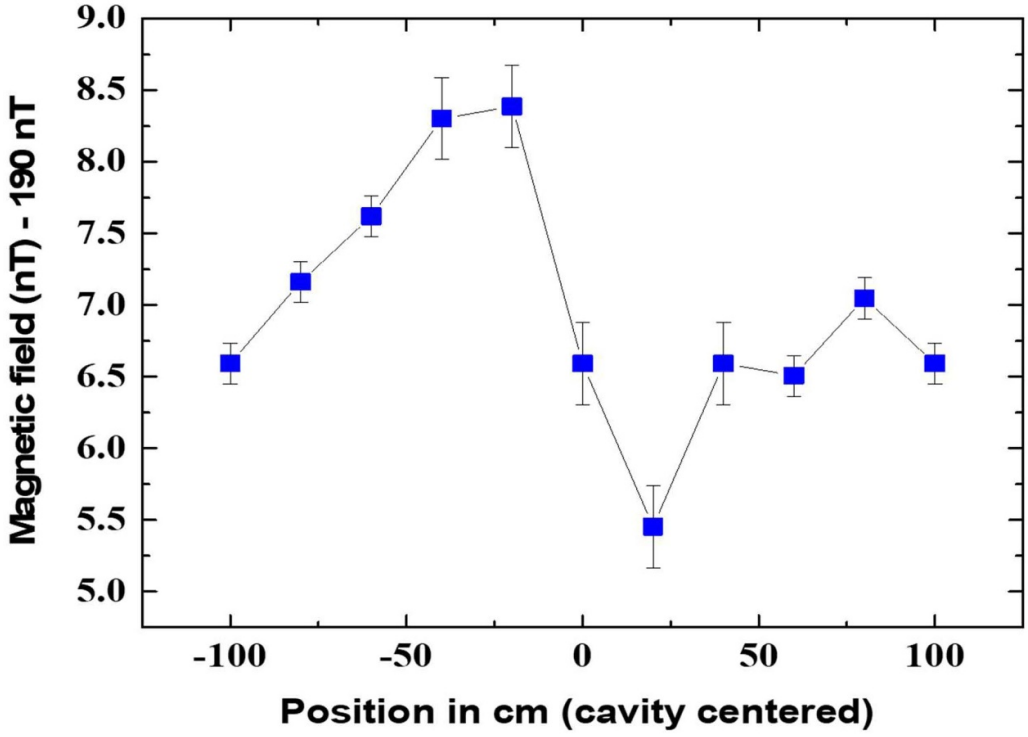

Figure 11. Magnetic field versus longitudinal position in the Ramsey cavity. RF Zeeman transitions are used to probe the field in the Ramsey flight region. First and the last points are from Rabi excitations in the first and second Ramsey interaction zones.

This gives a temperature of the thermal bath:

$$T = 0.007 \times T\text{capt} + 0.005 \times T\text{det} + (1 - 0.007 - 0.005) \times T\text{c}.$$

From this, we get a temperature uncertainty due to the external radiation of $\sigma_{\text{ext}} = 9$ mK.

The three contributions give a total BBR temperature uncertainty of $\sigma_c = \sqrt{\sigma_g^2 + 2 \times \sigma_p^2 + \sigma_{ext}^2} = 57\,\text{mK}$.

The blackbody radiation frequency shift is [36, 37]:

$$\frac{\Delta\nu}{\nu} = --1.710(0.006) \times 10^{--14} \left(\frac{T}{300}\right)^4 \left(1 + 0.013 \left(\frac{T}{300}\right)^2\right).$$

At 25 °C, ($T = 298.15$ K), the frequency shift is $\frac{\Delta\nu}{\nu} = -1.69 \times 10^{-14}$.

The temperature uncertainty contributes for $\pm 1.3 \times 10^{-17}$, and the uncertainty of coefficients, $\pm 6 \times 10^{-17}$, dominates. Note that the coefficient's uncertainty will not significantly degrade comparisons of PHARAO with primary Cs fountain clocks operating near 25 °C. Furthermore, the uncertainty of these coefficients may improve with more theoretical refinements or experimental measurements.

4.3. Cold collision frequency shift

The scattering of cold atoms produces a frequency shift proportional to the atomic density [38] and, for Cs, this shift strongly depends on the collision energy [39, 40]. To evaluate this shift, we measure the clock frequency at a high and low density, by selecting different numbers of atoms in the microwave selection cavity.

On Earth, we change the number of atoms by about a factor of two by varying the microwave frequency fed to the state preparation cavity. In this way, the atomic density changes without significantly changing the spatial distribution [41]. These measurements yield a fractional frequency shift of -4.3×10^{-21}/atom, with an uncertainty of 20% determined by the statistical uncertainty of the frequency measurements. During typical clock operation on Earth, the number of atoms after selection in $m_F = 0$ is 1.6×10^6, yielding a frequency shift of -6.9×10^{-15}, with a standard deviation of 1.2×10^{-15}. This agrees with previous measurements using the PHARAO engineering model, which had a frequency shift of $-5.3 \times 10^{-15} \pm 10^{-15}$ for 1.2×10^6 atoms [17].

The stability of the frequency shift depends on the atom number fluctuations and the detection noise. Both of these depend on the stability of the laser powers. With the orbital fluctuations, the powers of the capture and selection laser beams remain stable within 1%. The power of detection optical pumping laser fluctuates by 3%, but because the optical pumping is saturated, this minimally increases the detection noise. A servo loop stabilizes the other detection beam intensities to 10^{-4}.

Figure 13 shows the fractional Allan deviation of the detection signal. The orbital modulation produces a variation of 3×10^{-3}, consistent with the changes of the number of atoms due to the power fluctuations of the capture laser. Long-term

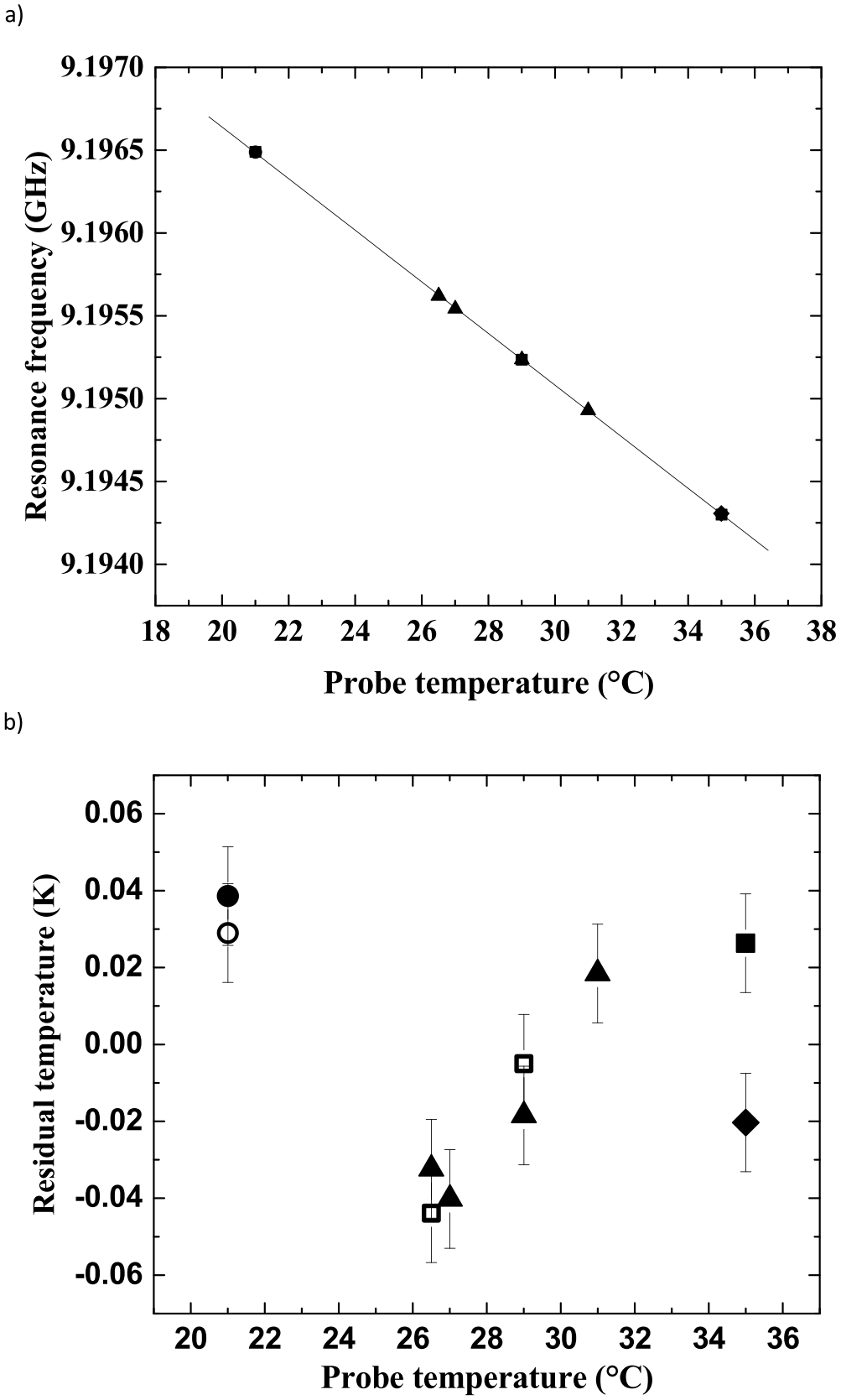

Figure 12. (a) Resonance frequency of the cavity as a function of the probe temperatures. (b) Residuals after the linear dependence is removed from the data. These residuals have $\sigma_g = 30$ mK. Baseplate temperatures are: circles 17 °C, triangles 23.5 °C, squares 27.5 °C and diamonds 29.5 °C. Temperature is modulated at the orbital period for the open points.

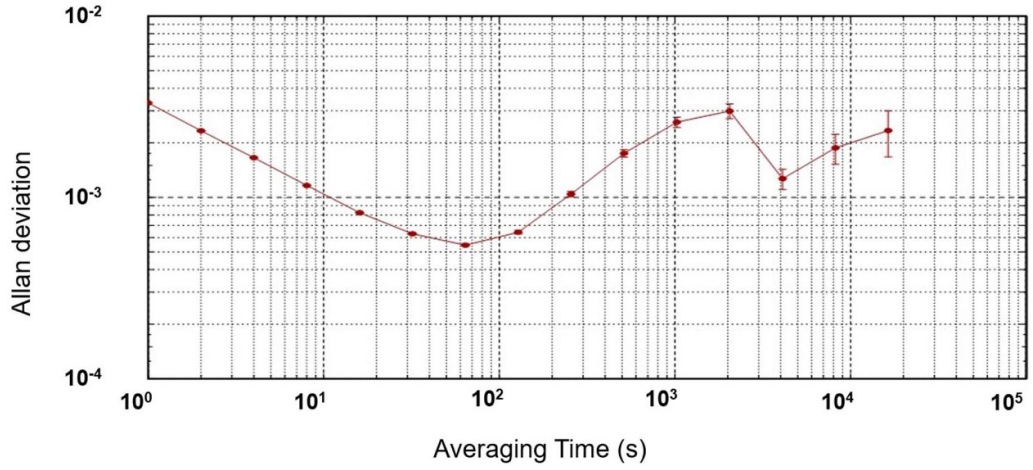

Figure 13. Allan deviation of the total detected signal. Modulation effect can be seen at the orbital period of 5400s.

drifts may exist, but an anticipated servo will control and balance the laser powers with 1% stability. The stability of the collision shift is therefore expected to be in the low 10^{-17} range.

Using our MonteCarlo model and for a clock operation on the ground, we calculate a frequency shift of -5.87×10^{-21}/atom using the collision shift rate coefficient from [40]. It is 20% larger, but consistent within the uncertainty on the initial cloud size and temperature. The calculated collision shift in microgravity versus launch velocity is shown in figure 14, as well as the number of detected atoms. The initial atom number is 2×10^7 and the microwave power is optimal, maximizing the amplitude of the Ramsey fringes. The frequency shift crosses 0 at a velocity of 260 mm s^{-1}. Here, the collision shift from $F = 3$ $m_F = 0$ population cancels the shift from the $F = 4$ $m_F = 0$ population, at 77 nK mean collision energy.

Since the Doppler shift also varies with the launch velocity, we plan to cycle between four launch velocities (large black circles in figure 14), with the maximum and a specific low number of atoms for each. As described in more detail below, this is likely to be performed throughout much of the mission duration to reach a statistical uncertainty below 7×10^{-17} of the frequency bias for a launch of 3×10^6 atoms at 198 mm s^{-1}, which simultaneously allows high accuracy and stability.

4.4. End-to-end and distributed cavity phase shifts

The desired microwave field is a pure standing wave with no phase variations to avoid Doppler shifts. The high but finite conductivity of the copper cavity walls leads to small losses and therefore the total microwave field has spatial phase variations. The difference of the effective phase [32, 33], for the ensemble on the cavity traversals, divided by the interrogation time T, yields an apparent first-order Doppler shift of the clock's frequency. These distributed cavity phase shifts have been and continue to be an important limitation to the accuracy of fountain clocks [42–46]. Here, we extend the treatment of cylindrical fountain cavities [32, 33], which has been stringently tested and widely used [26–28], to the rectangular cavity of PHARAO. The cylindrical symmetry of fountain cavities allows the field due to the losses, $\mathbf{g}(\mathbf{r})$, to be decomposed into an azimuthal Fourier series $\sum_m g_{z,m}(\rho,z)\cos(m\phi)$, where only m = 0,1 and 2 are significant [33]. The small m = 0 and 2 terms can be calculated and any unintended m = 1 phase gradients in the cavity are measured, for example by tilting the fountain to intentionally displace the atoms on the two cavity traversals [42–46]. Not only is the azimuthal Fourier series less natural for the rectangular cavity of PHARAO, it has two distinct Ramsey interaction zones instead of a single one in fountains. PHARAO therefore requires a new evaluation procedure because, for example, there could be different phase gradients in the two interaction zones and the atoms in PHARAO cannot be controllably and independently translated in both directions in each zone. The principle advantage of microgravity for laser-cooled clocks is long interrogation times, which dramatically reduce these Doppler shifts. In addition, in contrast to fountains, the launch velocity in PHARAO can be changed by an order of magnitude or more. Below, we discuss these and the other significant differences with fountains, including larger longitudinal phase gradients and frequency shifts from different microwave pulse areas in each Ramsey interaction zone. We show that the DCP frequency shifts can be evaluated using linear and quadratic extrapolations as a function of the launch velocity.

To study the potential phase distributions of the microwave field of the PHARAO Ramsey cavity, we developed a large 3D finite-element model (FEM). Many more computer resources, particularly memory, are required for 3D FEM than for the 2D models for fountains [14, 15]. The PHARAO cavity is 25 cm long and the microwave fields are nearly singular on the scale of the radii of sharp corners at the cavity apertures, which are likely as small as 20 μm. We therefore use a non-uniform and adaptive FEM mesh, meshing the atom interaction regions, particularly near the cavity apertures, more densely, with tetrahedra as small as 3.5 μm. The symmetry of the cavity was checked by measuring all dimensions with 5 μm resolution

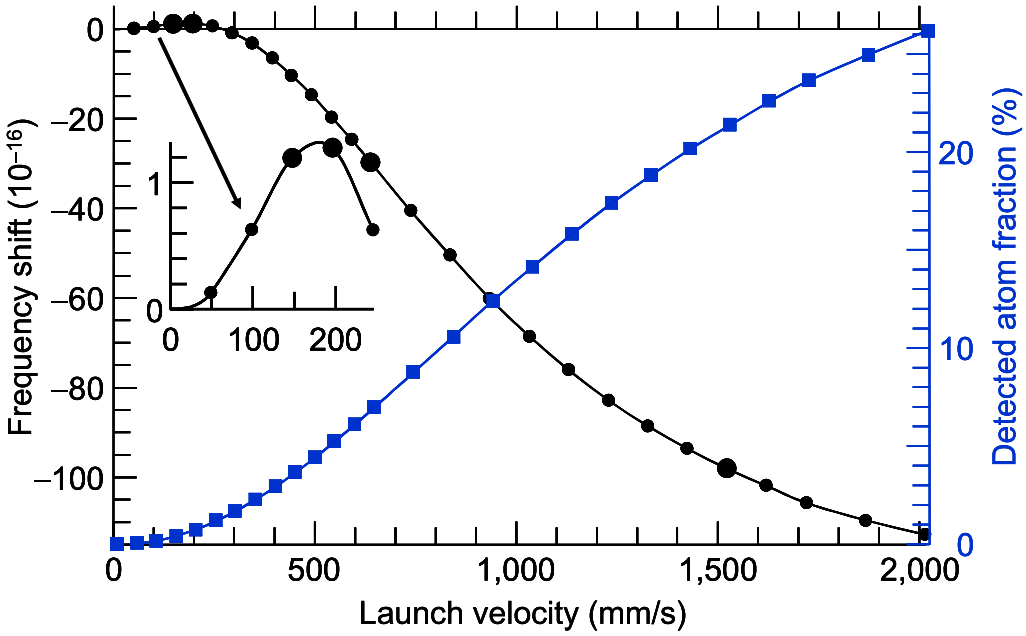

Figure 14. Calculated collisional frequency shift in microgravity (circles) versus launch velocity. Number of selected atoms is 1×10^7 and the velocity distribution is Gaussian with $\sigma(1D) = 10$ mm s^{-1}. Fraction of detected atoms is shown as blue squares.

and by measuring the amplitudes of several cavity modes with a small probe inserted into the cut-off waveguides of the cavity. This symmetry allows models that are symmetric, and also antisymmetric models in y and z (see figure 1), requiring four times less memory. Furthermore, by writing the field as a superposition $\mathbf{H}(\mathbf{r}) = \mathbf{H}_0(\mathbf{r}) + (\Delta\omega/\Gamma + \mathrm{i})\,\mathbf{g}(\mathbf{r})$, we can separately solve for purely real fields, the desired standing wave $\mathbf{H}_0(\mathbf{r})$ and the field due to the losses, $\mathbf{g}(\mathbf{r})$ [14, 15]. This further reduces the memory requirements by a factor of two, as compared to solving for complex fields and, more importantly, avoids significant errors in $\mathbf{g}(\mathbf{r})$ when $\mathbf{H}(\mathbf{r})$ is calculated directly, due to numerical imprecision in $\mathbf{H}_0(\mathbf{r})$ contaminating the much smaller $\mathbf{g}(\mathbf{r})$. This, along with the availability of much more computer RAM, has yielded significantly more accurate FEM fields than those of an early FEM calculation for the PHARAO cavity [17]. The boundary condition for $\mathbf{H}_0(\mathbf{r})$ on the copper walls is a perfect conductor, with no electric field parallel to the surface. For $\mathbf{g}(\mathbf{r})$, the boundary condition on the walls is given by the parallel component of $\mathbf{H}_0(\mathbf{r})$ and the amplitude of the exciting cavity feed [32, 33]. Our final mesh has 27 million tetrahedra and uses nearly all of our 1TB of available RAM, requiring several hours to solve with 32 processor cores.[2]

Figure 15 shows the calculated FEM fields in one interaction zone, $H_{0x}(\mathbf{r})$ and the loss field $g_x(\mathbf{r})$, which is of the order of 10^4 times smaller than $H_{0x}(\mathbf{r})$. The near singularities of $H_{0x}(\mathbf{r})$ and $g_x(\mathbf{r})$ are due to large currents at the apertures of the cavity [32, 33]. The gradient of $g_x(\mathbf{r})$ along x is due to power being fed into the interactions zone from the center of the cavity (see figure 2), here, from positive to negative x, and in the opposite direction in the other Ramsey zone. The cavity symmetry yields gradients with opposite signs in the two Ramsey zones. These fields are symmetric in y by construction, and are nearly symmetric in z.

The cavity phase perturbations in figures 16 and 17 are calculated with a Monte Carlo simulation that extends our previous treatment for fountains and which was verified by several clock measurements [42–46]. We model the atomic cloud size, temperature, all the apertures defining the atomic trajectories and the selection and detection probabilities. We allow for cloud offsets, tilts of PHARAO relative to gravity on the ground, and launch angle misalignments. Below, we show both frequency shifts δv due to cavity phase and the related perturbation of the transition probability δP, where, for $\pi/2$ pulses, $\delta v \approx 2\ \Delta v\ \delta P/\ \pi$ and Δv is the resonance linewidth.

Figures 16(a) and (b) show δP versus microwave amplitude b in microgravity due to known cavity wall losses. This corresponds to the sum of the $m = 0$ and $m = 2$ DCP contributions for fountain clocks [33] [42–46]. Similar to fountains, the frequency shifts are large near $b = 4$ and 8 but, due to the longitudinal phase gradient along x, δP also has a peak at $b = 2$ in contrast to fountains. The opposite sign of the shifts at $b = 2$ and 4 would similarly occur in fountains if a fountain cavity was fed from the top end-cap instead of at the midplane. At optimal amplitude, the frequency shift is negligibly small, -0.05×10^{-16} for a launch velocity $v = 0.148$ m s^{-1}. In figure 16(a), δP changes, albeit slowly, with the launch velocity because the cloud expands more for low launch velocities, and therefore the transverse positions of the atoms in the two Ramsey zones are less correlated [33]. Figure 16(b) shows that a small difference in the amplitude of $H_{0x}(\mathbf{r})$ in the two Ramsey zones can lead to significant frequency shifts. On the basis of dimensional measurements, the field amplitudes are believed to differ by much less than ±5%.

[2] COMSOL was used for these calculations.

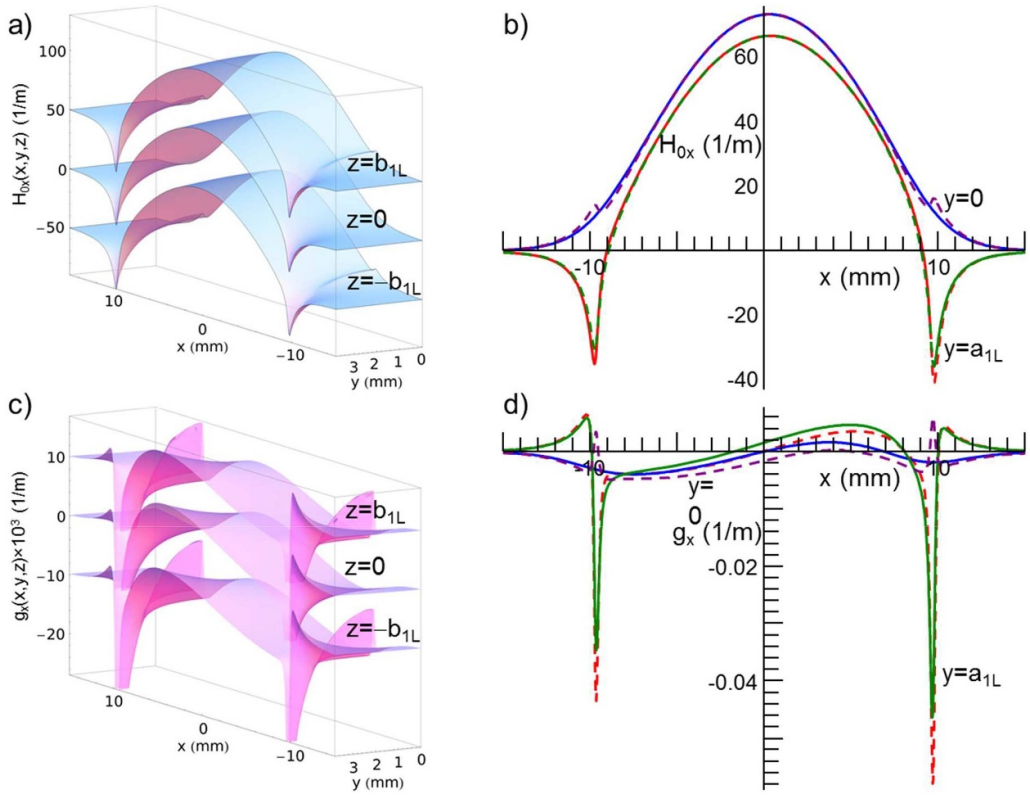

Figure 15. Microwave field of the Ramsey cavity of PHARAO in the first Ramsey zone. (a), (b) Standing wave field is $H_{0x}(r)$ and (c), (d) the smaller field due to the losses and cavity feed is $g_x(r)$. Surface plots depict the field for three different z and the linear plots two values of y and z, where a_{1L} and b_{1L} are the dimensions of the masks, 3.8 and 4.3 mm. Fields are almost singular near the apertures of the cavity. In (b), the solid (dashed) curves are for z = 0 (4.3 mm) and y = 0 and 3.8 mm. Surfaces in (a) and (c) for $z = \pm b_{1L}$ are offset vertically and here x is relative to the center of the first interaction zone, which is −109.5 mm from center of the cavity (see figure 2).

On Earth, the DCP shift is dominated by the longitudinal phase gradient, combined with a difference in pulse areas in the two zones due to gravity changing the atomic velocity. Figure 16(c) shows the shift's large dependence on the microwave amplitude *b*. The longitudinal phase gradient is 9 μrad mm^{-1} at the center of each interaction zone and the cavity symmetry gives gradients with opposite signs in the two zones. The large frequency shift results from gravity slowing the atoms between the two Ramsey interactions so that the second Ramsey pulse has a significantly larger pulse area. The calculated frequency shift agrees with the measurements (red points) in figure 17(d) and is 2.4×10^{-15} at optimum microwave amplitude. If the pulse areas are equal for both zones, the '0g' calculation in figure 16(c), the frequency shift from these longitudinal phase gradients is dramatically smaller. Even small differences of the pulse areas in the two zones, ±5%, albeit much larger than expected, give noticeable frequency shifts.

The range of available launch velocities in microgravity leads not only to smaller cavity phase frequency shifts than on Earth, but also enables their evaluation. Figure 17(a) shows δP at optimal amplitude ($b \approx 1$) versus launch velocity. It is nearly constant as expected, with a small but abrupt deviation below 0.2 m s^{-1} due to the Coriolis acceleration on the 90 min orbit. A constant δP yields a shift δv that is linear in v, as shown for a nearly constant δP in figure 17. For these DCP shifts, as well as for unintended phase gradients discussed below, we show that linear and quadratic extrapolations of the DCP frequency shifts versus launch velocity can be used to evaluate the DCP shift and its uncertainty in microgravity. In figure 17(b), we show the linear (solid) and the quadratic (dashed) extrapolations of the clock frequency to zero velocity. A good solution that offers high stability and accuracy uses velocities of $v_3 = 3 \times 0.0492$ m s^{-1} = 0.1476 m s^{-1}, $v_{13} = 13 \times 0.0492 = 0.6396$ m s^{-1}, and $v_{31} = 1.5252$ m s^{-1}, where the linear extrapolation uses only the two lowest velocities. The frequency shifts from both extrapolations remain lower than 10^{-16} and lead to a negligible uncertainty, less than 10^{-17}, even for large ±5% differences of pulse areas. End-to-end cavity phase shifts produce a strictly constant δP and linear δv, and therefore are automatically evaluated with these extrapolations. We next analyze the DCP extrapolations versus launch velocity for unintended phase gradients, postponing until the next section a discussion of the optimization of the time spent at each velocity and number of atoms to evaluate the combined cavity phase and ultracold collision shifts in orbit.

Frequency shifts result from unintended transverse phase gradients. For example, small differences in the surface resistance of the clock cavity lead to more wall losses on one side of the cavity. We simulate such a potential phase gradient in our FEM with a 10% difference in the surface conductivity for the

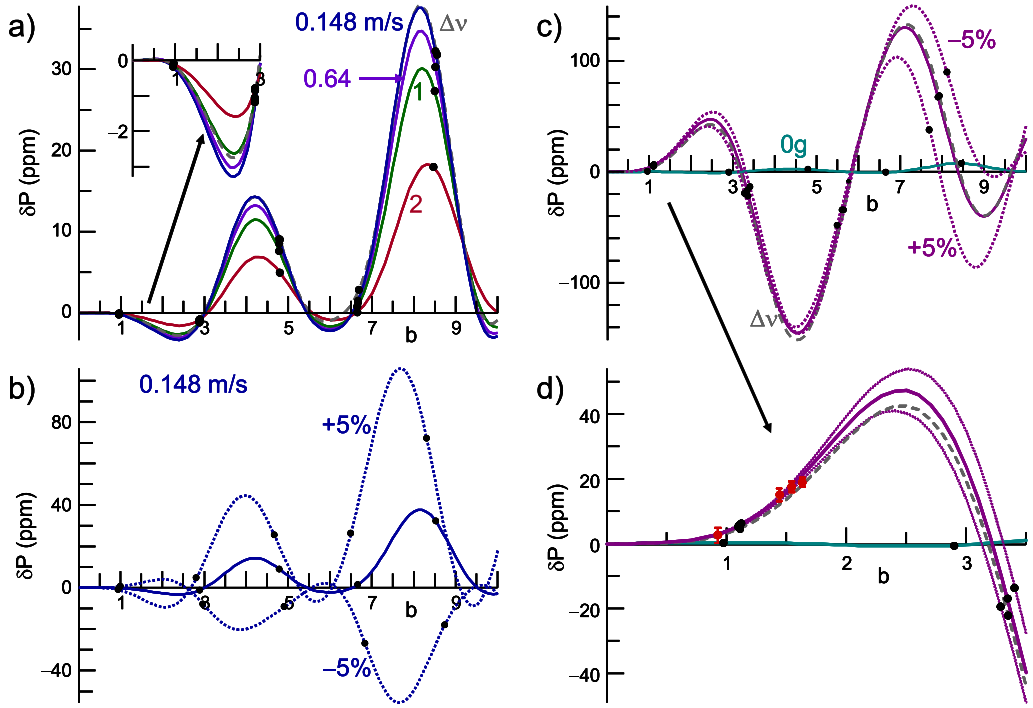

Figure 16. Perturbation of the transition probability δP due to cavity phase variations versus microwave amplitude b (a), (b) in microgravity and (c), (d) on Earth. (a) δP in microgravity for $v = 0.1$–2 m s^{-1}. (c) On earth, the pulse area in the second Ramsey zone is larger, which leads to large frequency shifts compared to the shifts for equal pulse areas '0 g.' (d) Measured red points agree with the expected DCP shift, where the frequency offset at optimal power, $b = 1.109$, is taken to be the calculated shift. In (b), (c) and (d), we show the shift for a 5% difference in pulse areas in the two Ramsey zones (dotted). Black dots indicate optimal microwave amplitudes for $n = (1,3,5,7,9)\pi/2$ pulses. Curves Δv (gray dashed lines) depict the calculated shifts for a cavity detuned by 240 MHz, which gives small differences.

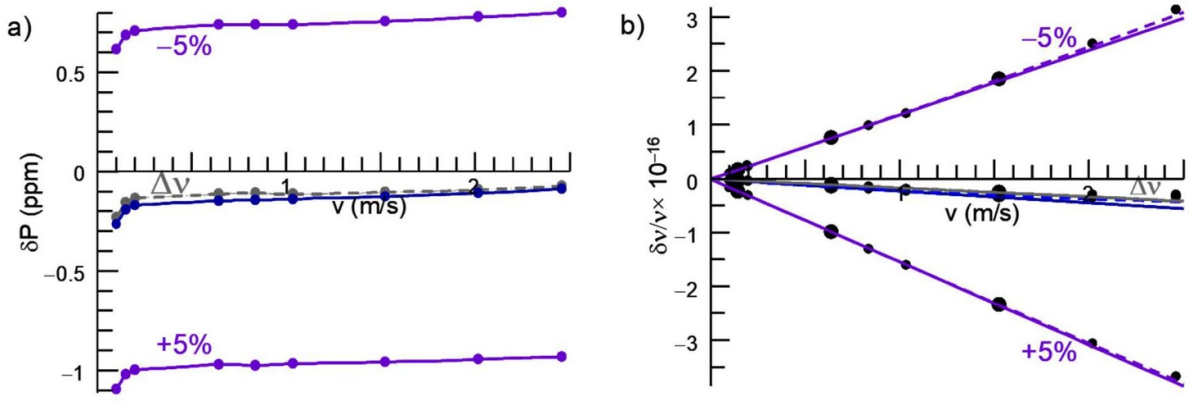

Figure 17. δP versus launch velocity, for a resonant and detuned clock cavity, as well as for 5% differences of Ramsey pulse area. The δPs are fairly constant, except at small velocities where the Coriolis acceleration significantly deflects the atomic trajectories. (b) Linear (solid) and quadratic (dashed) frequency extrapolations versus velocity lead to differences much less than 10^{-16} and negligible systematic uncertainties. Quadratic extrapolation uses three velocities (see text), $v_3 = 3 \times 0.0492$ m s^{-1} $= 0.148$ m s^{-1}, $v_{13} = 0.640$ m s^{-1} and $v_{31} = 1.525$ m s^{-1}, depicted as the large points, and the linear uses only v_3 and v_{13}.

left and right sides, or top and bottom of the cavity. Although the top/bottom differences produce negligible phase gradients, a 10% left/right resistance asymmetry produces a phase gradient of $d\Phi/dy = 66$ μrad mm^{-1} and significant frequency shifts. In contrast to fountains, these unintentional transverse phase gradients will generally be different in the two Ramsey zones, so we consider each zone separately. Figures 18(a) and (b) show δP and δv for a phase gradient $d\Phi/dy$ in the first Ramsey zone for 2 mm cloud offsets on the y axis, as well as launch angle errors of 1mrad. The δPs for these vary approximately linearly with velocity and therefore δv has a nearly quadratic dependence. Note that a non-zero frequency shift exists for a non-zero $d\Phi/dy$ even for centered atom trajectories (no offset or launch angle) at low launch velocities, since the opposing gradients of the fluorescence collection do not precisely cancel. This occurs because the atoms spread as they travel

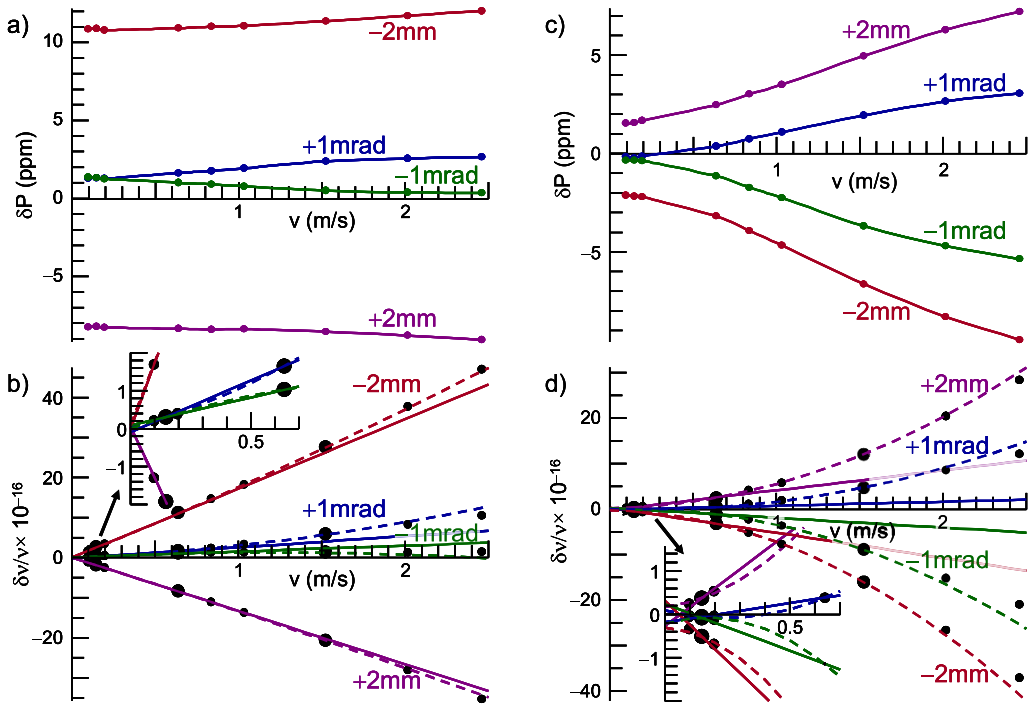

Figure 18. (a) δP and δv versus launch velocities for phase gradients dΦ/dy in the (a), (b) 1st and (c), (d) 2nd Ramsey zone due to inhomogeneous wall resistances and cloud offsets of $y = \pm 2$ mm or launch angles of ± 1 mrad. δPs vary smoothly with launch velocity for cloud offsets and launch angle misalignments. For non-zero launch angles, δP varies approximately linearly with velocity for moderate velocities. (c), (d) Linear (solid) and quadratic (dashed) frequency extrapolations for three launch velocities, v_3, v_{13} and v_{31}, lead to extrapolated frequency errors less than 10^{-16} in the insets.

from the F = 4 detection zone to the F = 3 zone, making the $F = 3$ fluorescence collection gradient effectively larger than the F = 4 gradient. Although the DCP frequency shifts can be significantly larger than 1×10^{-16}, the linear and quadratic extrapolations versus launch velocity determine these frequency shifts with sufficient accuracy, lower than 10^{-17} (see inset of figure 18(b)).

Figures 18(c) and (d) similarly show δP and δv for the same phase gradient dΦ/dy in the second Ramsey zone. The frequency shifts can be significant and the inset of figure 18(d) shows that the linear and quadratic extrapolations to zero velocity can be slightly different; their mean is zero within 1×10^{-17} and their difference is also small. We have examined a number of other effects, including potential unequal detection gradients and selection cavity inhomogeneities [25]. We expect that these phase gradients, cloud offsets and launch angle errors are upper bounds of the asymmetries of PHARAO. All calculations show that a mean of the linear and quadratic extrapolations can be taken as the clock frequency, within an uncertainty of ¾ of their difference, which we take as the systematic uncertainty. Contingent upon measurements in orbit showing smaller DCP shifts versus launch velocity than the above examples, systematic DCP uncertainties below 7×10^{-17} are expected.

To check that there are no anomalous phase gradients, a number of frequency measurements were made on the ground. The longitudinal phase gradients were measured with only one interaction zone (Rabi pulse). At optimum microwave power (π pulse), the measured frequency shift was 4.1 (1) mHz for the first zone and −2.85 (10) mHz for the second zone. The calculated frequency shifts are 3.6 and −2.6 mHz respectively. For the Ramsey pulses, we predict a frequency shift of 2.4×10^{-15} at optimum microwave power. We also observe the predicted large sensitivity (figure 16) to the microwave field amplitude (7×10^{-16} for a 10% variation). The clock was also tilted by ±20 mrad along two perpendicular axes with the FOM fountain serving as a frequency reference. No frequency shift was seen with a resolution of 2×10^{-15}. For ground operation, we attribute a conservative DCP uncertainty of 1.3×10^{-15}.

In contrast to our FEM calculations of fountain cavities, our PHARAO models do not precisely reproduce the measured Ramsey cavity resonant frequencies and the reflection spectrum from the coupling cavity. We have not identified the origin of these differences. We therefore also show calculated frequency shifts for a cavity detuned by 240 MHz; the gray dashed curves in figures 16–18. The effect of the cavity detuning is small and is accounted for by the extrapolation to zero launch velocity.

4.5. Combined DCP and cold collision shift evaluation

The efficacy of the above DCP evaluation relies on removing the collision shift, and other velocity dependent shifts that are not proportional to velocity (e.g. microwave lensing), before extrapolating to zero launch velocity. The cold collision shift evaluation is itself an extrapolation of the clock frequency, to zero atomic density, using a high and low number of atoms

at each launch velocity. Therefore, the combined DCP and cold collision shift is extrapolated in two dimensions, based on three launch velocities and two atom numbers, as depicted in figure 19.

With the projected clock instability in figure 7, including its dependence on the quantum projection noise versus atom number, we can optimize the averaging time spent at each density for the three launch velocities to evaluate the combined DCP and cold collision shift. The instabilities of the extrapolations benefit from a large spread in velocities, provided the DCP frequency shifts remain linear and quadratic, and particularly a high stability at the lowest velocity. Operating PHARAO in this way, these traditionally systematic frequency shifts become statistical uncertainties that contribute to the clock's instability and, as the clock runs in space, they become better and better determined. The resulting velocity extrapolation of the clock's frequency, the mean of the linear and quadratic extrapolations, can have an instability of $5 \times 10^{-13}\ \tau^{-1/2}$, which would reach 10^{-16} in 10 months of averaging. The instability of the combined DCP and collision shift, ¾ of the difference of the linear and quadratic extrapolations, is smaller, $1.2 \times 10^{-13}\ \tau^{-1/2}$, reaching 10^{-16} in 18 d. However, the instability of the extrapolated clock frequency is insufficient to meet the time-transfer goals during the planned approximately 20 d long dedicated sessions. Therefore, PHARAO can instead operate with a reasonably high stability of $1.5 \times 10^{-13}\ \tau^{-1/2}$ at a single launch velocity of $v_4 = 196$ mm s^{-1} with $N_4 = 30\%$ of the atoms selected, during the dedicated time-transfer sessions and then evaluate the DCP and cold collision frequency shift correction for that operating point over a period of months.

Figure 19 shows an optimization for the evaluation of DCP and cold collision frequency shift correction for operating at O4 $\equiv (v_4, N_4)$, with a launch velocity of $v_4 = 196.8$ mm s^{-1} and selecting $N_4 = 30\%$ of the atoms. The leverage of the large velocity in the DCP extrapolation means that little stability is required for $v_{31} = 1.53$ m s^{-1}, indicated by the size of the circles, whereas high stability at $v_3 = 0.148$ m s^{-1} significantly reduces the instability of the correction. Therefore, it is optimal for PHARAO to spend most of the time at low launch velocities and low atom numbers to evaluate the combined DCP and cold collision shift correction of the operating point O4. Since the short-term stability improves with higher atom numbers, it is optimal to use all of the atoms, $N_H = 100\%$, along with a small number, $N_L = x\%$, to evaluate the collision shift at each velocity v_j. We arrive at a sequence that spends half of the evaluation time averaging at E1L(v_3, $N_L = 20\%$), 1/16 of the time at E1H(v_3, N_H), 9/32 at E2L $\equiv$ (v_{13}, 17%), 1/32 at E2H(v_{13}, N_H), 9/320 at E3L $\equiv$ (v_{31}, 15%), 1/320 at E3H $\equiv$ (v_{31}, N_H), and, to evaluate the collision shift at v_4, 3/32 of the time at E4H(v_4, N_H). This sequence can be formed by eight sets of four configurations, where each configuration is E1L, E2L, E1L, X, where X cycles through the other evaluation points including a ninth instance of E1L and a combined E3L and E3H. This can determine the DCP and cold collision shift correction at O4 (red dot in figure 19), with an instability of $3.8 \times 10^{-13}\ \tau^{-1/2}$, to 10^{-16} within 6 months of averaging. The instability of the systematic error of the DCP and collision shift correction at O4 is significantly smaller, $1.3 \times 10^{-13}\ \tau^{-1/2}$. We note that this procedure does not preclude the long-term extrapolation of the clock's frequency described above using only v_3, v_{13} and v_{31}, now slightly compromised to take nearly 1 year with an extrapolated instability of $5.5 \times 10^{-13}\ \tau^{-1/2}$. We anticipate adding one instance of O4 to each set, e.g. E1L, E2L, E1L, X, O4 to make eight sets of five configurations, for the first couple of months, and then potentially to operate as much as half of the time at O4 for much of the ACES mission, outside of the dedicated time-transfer sessions. This allows an evaluation of the DCP and collision shift with a small uncertainty, below 7×10^{-17} during the planned ACES mission.

4.6. Microwave lensing frequency shift

During the microwave interactions in the Ramsey cavity, the curvature of the atoms' dipole energy in the standing wave of the Ramsey cavity exerts small forces on the atoms. The forces in the first Ramsey zone act as a lens on the atomic wave functions, focusing one dressed state and defocusing the other [47]. In PHARAO, four apertures clip the atomic trajectories and lead to the microwave lensing shift. The shift and its sensitivity to the clock's and parameters were analyzed in [25]. The calculated shift is 11.6×10^{-17}, and can vary by as much as $\pm\ 3 \times 10^{-17}$, for example, for significant changes of the atomic cloud parameters. A conservative uncertainty of $\pm 4 \times 10^{-17}$ is expected.

4.7. Light shifts

The atomic preparation and detection use two 852 nm lasers that are nearly resonant with the $6s_{1/2}$ F = 4→$6p_{3/2}$ F' = 5 and F = 3→F' = 4 transitions. Stray laser light can produce a clock frequency error due to the AC Stark shift, or light shift, during the Ramsey interrogation. In the laser source subsystem, the beams are switched off by successively turning off the RF power of AOMs and closing mechanical shutters. We have measured the extinction ratio at the fiber outputs with heterodyne measurements and a photo-multiplier tube. The AOM attenuations reach −60 dB after 100 µs and the shutter attenuation is below −120 dB after 1 ms, limited by the measurement noise. The light shift is $(\Gamma^2/4\delta)$I/Is, where $\Gamma = 5$ MHz is the natural linewidth of the excited $6P_{3/2}$ state and δ is the detuning. With 120 dB of attenuation, the frequency shift is 6×10^{-18}. In orbit, the scale of the light shift can be verified by leaving the shutters open and changing the AOM RF powers during the interrogation time.

4.8. Frequency shifts from background gas collisions

The collision of the cold atoms with the background gas has been theoretically analyzed in [48]. The important result is that a pressure of 2×10^{-8} Pa results in a frequency shift of the order of -4×10^{-18}, which is proportional to the loss of cold atoms during the microwave interrogation. The vacuum inside the Cs tube is evaluated to be 2×10^{-8} Pa from measuring the ion pump current. This calibration was performed with the vacuum chamber connected to an external pumping

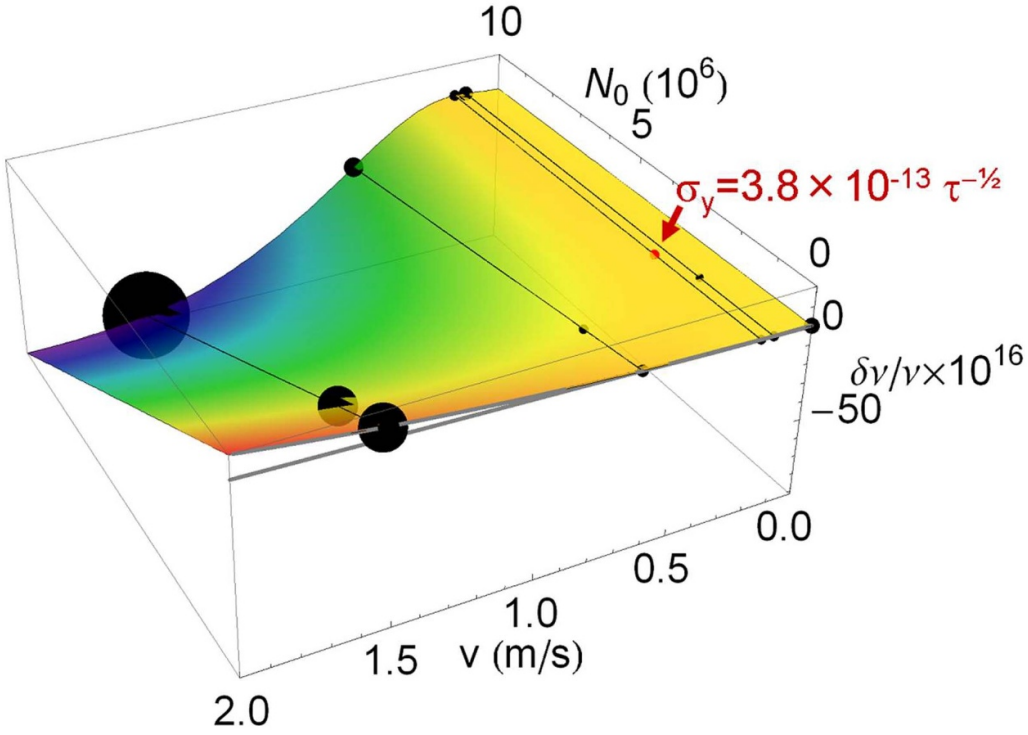

Figure 19. Combined extrapolation of cold collision and DCP frequency shifts versus atom number and launch velocity. This example DCP shift is the curve for a 2 mm cloud offset in figure 18(b). Optimizing the fraction of time spent at each point yields an uncertainty at each (v_j, N_0) point, which is shown by the diameter of the black circles. These yield a cold collision shift correction and uncertainty at each velocity, and these in turn give a DCP correction and uncertainty, extrapolated to ($v = 0$, $N_0 = 0$) and to an operating point O4 ≡($v_4 = 0.1968$ m s^{-1}, $N_0 = 3 \times 10^6$). Instability is low at O4, 1.5×10^{-13} $\tau^{-1/2}$, and the instability of the DCP and cold collision shift correction here is 3.8×10^{-13} $\tau^{-1/2,}$ allowing the combined correction uncertainty to be evaluated to $\pm$ 7 $\times$ 10^{-17} during the ACES mission.

system with several gauges, gate valves and a gas analyzer. The Cs vapor pressure in the capture zone is 2–3 $\times$ 10^{-6} Pa and is rapidly attenuated by a series of apertures and graphite tubes. Five getters are also arranged in the interrogation zone. The density of the Cs thermal beam in the interrogation zone falls to 3.5% of the density in the capture zone. Consequently, we expect a frequency shift of about -2 $\times$ 10^{-17}. During the space mission, it will be possible to determine the loss of cold atoms by changing both the Cs pressure (10^{-7} to 10^{-5} Pa) and the loading time to keep the same initial atom number (given by the fluorescence measurement) and evaluate the shift from background Cs atoms [49].

4.9. Frequency shifts from neighboring transitions

Nearby atomic microwave transitions produce the Rabi and Ramsey pulling. These are generally negligible for cold atom clocks because the atoms in $m_F \neq 0$ Zeeman substates are cleared from the clock and the resonance widths are much narrower than the Zeeman splitting. In [50], the authors have extensively analyzed these effects in a Cs fountain, performing simulations and measurements. They highlight the importance of having balanced $\pm$ m_F populations and preparing the initial clock state without off-diagonal coherences. After the PHARAO state selection, 98.5% of atoms are in the F = 3 $m_F = 0$ level. The remaining 1.5% of atoms are in F = 3: 1% are launched from the capture zone and 0.5% are generated by the optical pumping (F = 4 to F = 3) in the pushing laser beam. The population imbalance between the $m_F = \pm 1$ states is less than <1% and the Zeeman splitting is ten times the resonance linewidth. From [50], the frequency shift due to the other lines is expected be less than 10^{-16}. In microgravity, we plan to use the same magnetic bias field in the state preparation cavity, further suppressing off-resonant transitions, since the state-preparation linewidths will be ten times narrower during normal operation.

4.10. Frequency shifts due to microwave leakage

Resonant microwaves outside the cavity perturb the hyperfine coherence and produce a potential shift of the clock frequency. Such a microwave field can come from leakage between the microwave source and the cavities. The leakage of the microwave cavities and coaxial cables has been evaluated with a horn antenna and a heterodyne detector. No microwave signal was detected with a resolution of −120 dB of the power fed to the cavities. Further investigation has used vacuum leak detection to search for cracks in the cavity walls and in the cable jackets (with the cut-off waveguide sections sealed for these measurements). No leaks were detected. The early FEMs of the interrogation and preparation cavities give a microwave attenuation of −200 and −150 dB, respectively. In addition, during clock operation the microwaves fed to the preparation

cavity are attenuated by −80 dB after the atoms leave the cavity, significantly reducing potential leakage.

The total leakage of the microwave source has been measured to be −97 dB of the field injected into the cavity. The coaxial cable of the Ramsey cavity is brazed to the vacuum chamber where the jacket passes through the chamber to ensure the vacuum seal and grounding. The cable is connected to the microwave source outside the outer magnetic shield of the Cs tube, which is constructed to also serve as an electromagnetic shield. To prevent possible stray microwaves from entering the vacuum chamber, the windows are surrounded by optical collimators that are designed to shield RF and microwave fields. In addition, there are two microwave cut-off waveguides along the atomic path, between the preparation and the interrogation zones and between the interrogation and the detection zone. Accordingly, we do not expect significant frequency shifts due to microwave leakage. In orbit, to check for microwave leakage and other systematic effects, the microwave power will be changed by orders of magnitude and the observed frequency shifts will be compared with those from simulations.

4.11. Microwave spectral purity

Spurious intensity peaks in the microwave spectrum can also produce frequency shifts of the clock. The measurements of the microwave spectrum show two lines close to the carrier, with offsets of 25 and 50 Hz, at a level of −70 dBc, likely due to the power supply used for these measurements. The other lines are far from all of the atomic resonances and Ramsey cavity resonances. They are below −60 dBc, except for three lines at offsets of 7.5, 68 (−38 dBc) and 392 MHz (−28 dBc). All the lines thereby produce negligible AC Zeeman shifts.

The largest concern is phase changes between the 100 MHz signal and the 9.2 GHz signal stabilized to the atoms. The 100 MHz signal, which will define the ACES timescale, is phase-locked to the hydrogen maser. The environmental sensitivity of the microwave synthesis that connects 100 MHz to 9.2 GHz has been measured to be −2.1 ps $^{\circ}C^{-1}$ and at 200 fs mT^{-1}. Neglecting the magnetic sensitivity, the thermal component can induce a frequency modulation of -5.8×10^{-16}, synchronous with the orbital period. But, these are asynchronous with the observations of ground stations rotating with the Earth, so the modulation for the time comparisons will average over several orbits. Furthermore, the temperature telemetry, with 10 mK resolution, will allow the correlation to be verified, and potentially corrected.

Although the microwave signal to the Ramsey cavity is not switched during normal operation, there are some events that are synchronous with the clock cycle that modulate the microwave phase: communications with the computer, frequency changes for successive launches and especially the switching of the state preparation microwaves. The phase deviations of the 100 MHz and 9.2 GHz signals, relative to our cryogenic oscillator, have been recorded synchronously with the clock cycle and averaged to reach a noise floor of 1 μrad at 9.2 GHz. The phase of the 9.2 GHz jumps by about 25 mrad when the state preparation microwaves are switched. The phase excursion is strongly damped, with a 6 ms time constant, and the phase reaches our noise floor safely before the atoms enter the Ramsey cavity.

The 100 MHz signal similarly has a brief phase jump of 0.7 μrad when the state preparation microwaves are switched. In addition, a magnetic coupling between the quartz oscillator and a mechanical shutter of the laser source induces a small 0.2 μrad phase perturbation during the detection of the atoms. This phase jump *a priori* has no effect, since they follow the atomic interrogation time. However, they do contribute to the error signal of the phase lock loop for the hydrogen maser. Through the loop integrator, they induce a synchronous phase drift of the 9.2 GHz signal. The resulting clock frequency shift is estimated to be -3×10^{-17}. During the mission, the phase measurements between the 100 MHz PHARAO and the hydrogen maser will be transmitted via the telemetry. Averaging the phase behavior during the atomic interaction will allow the frequency shift to be measured and corrected.

4.12. Cavity pulling

The positive frequency detuning of the Ramsey cavity resonance (9.196 GHz) leads to a pulling of the clock's frequency from the oscillating magnetic dipole moments of the atom during the Ramsey interactions. On the ground the number of atoms is larger than in orbit and change the phase of the microwave field in the first Ramsey interaction to shift the clock's frequency [51, 52], by an estimated -7.8×10^{-17}. The second Ramsey interaction zone produces no pulling for $\pi/2$ pulses and, in orbit, the number of atoms and pulling is smaller. Because the cavity pulling and the cold collision shift are proportional to the atomic density, the extrapolation of the clock's frequency versus density accounts for both.

Another effect is the relative variation of the microwave amplitude with the frequency modulation (±2.8 Hz), which produces a second-order frequency shift. The Q factor of the cavity is low (1000) and therefore the relative amplitude modulation is only 2.10^{-6}. No frequency variation larger than 10^{-18} is expected.

5. Conclusion

The flight model of the space clock PHARAO has been qualified to operate in the framework of the ACES mission. The performance tests began with the Cs tube connected to the engineering model sub-systems to analyze the thermal accuracy and magnetic attenuation. This was followed by 4 months of operation with the entire flight model. Table 1 summarizes the accuracy budget of PHARAO on the ground and the expectation in orbit. The total uncertainty on the ground is 18×10^{-16}, mainly limited by the collision and the Doppler shift uncertainties.

The difference between PHARAO and the mobile fountain FOM has been measured to be 7×10^{-16}. This difference

Table 1. Uncertainty budget for PHARAO on Earth and in space. The uncertainty of the combined collision shift and first- order Doppler shift is expected to be predominantly the statistical error of the applied correction (see text). The systematic error will be determined in orbit. It has a smaller instability of 0.23×10^{-16} year$^{-1/2}$, and is expected to be less than the instability of the correction for a several-year mission duration.

	Ground operation		Space operation (prediction)	
Contribution	Frequency shift 10^{16}	Uncertainty 10^{-16}	Frequency shift 10^{16}	Uncertainty 10^{-16}
Second-order Zeeman	1811.0	0.1	900	0.1
Blackbody radiation	−171.7 (26.2 °C)	0.7	−169.0 (25 °C)	0.7
Cold collision and cavity pulling	−69	12	+1 (launch 196 mm s^{-1})	0.7 year$^{-1/2}$ (statistical)
First-order Doppler	27	13	0.4	
Microwave lensing	1	1	1.14	0.4
Light shift	0	0	0	0
Microwave leakage	0	0.1	0	0.1
Background gas collision	−0.1	0.2	−0.1	0.1
Rabi and Ramsey pulling	0	1	0	0.1
Microwave phase transients	−0.3	2	0.1	0.2
Total	1597.9	18	733.5	1.1

is well below the statistical uncertainty of the measurement 18x10^{-16} and the accuracy uncertainty (7×10^{-16} for FOM).

In space, several systematic effects will be lower. The second-order Zeeman shift uncertainty will be less, since a smaller magnetic field is needed to resolve the Zeeman levels. The cold collision and DCP frequency shift nearly vanish at low launch velocities. We estimate a total frequency uncertainty of 1.1×10^{-16} for the clock operating in microgravity. We note that the dominant contribution of the BBR uncertainty comes from the coefficient of the equation, converting the temperature measurement to a frequency shift. For frequency comparisons with Cs clocks operating near 25 °C, only the temperature uncertainty has to be taken into account. This reduces PHARAO's uncertainty to 0.86×10^{-16}.

The PHARAO clock has been delivered to ESA for the assembly of the entire ACES physical package. After the other sub-systems are delivered, the remaining main tests will be dedicated to the phase behavior of the generated timescale in the simulated orbital environment. The objective is to preserve a time stability of 10 ps over several days. Its launch into space is scheduled for mid-2021 with a Space X rocket.

Acknowledgments

We acknowledge financial support from CNES, CNRS, LNE, NASA and Penn State. The laser source and the Cs tube have been manufactured and qualified by Sodern, the microwave source by Thales Defense Mission systems (formerly Thales Airborne systems), the computer by EREMS and the software by Communication & Systèmes, under CNES contracts. We thank C Escande, P Lariviere, S Beraud and D Rovera for their contribution to the integration and test of PHARAO. We are grateful for the outstanding work assembling and testing the PHARAO flight model by all the members of the PHARAO industrial team at CNES: Ph Chatard, C M de Graeve, S Tellier, C Stepien, L Fonta, T Basquin, A Ratsimandresy, S Julien and E Leynia de la Jarrige.

Finally, we particularly remember two of our colleagues and dear friends, André Clairon, who was at the core of many aspects of the PHARAO project, and Jocelyne Guéna, who made many contributions to microwave fountain clocks, including her precise measurements of distributed cavity phase shifts.

References

[1] Kastberg A, Phillips W D, Rolston S L, Spreeuw R J C and Jessen P S 1995 Adiabatic cooling of cesium to 700 nK in an optical lattice *Phys. Rev. Lett.* **74** 1542–5
[2] Leanhardt A E *et al* 2003 Cooling Bose–Einstein condensates below 500 picokelvin *Science* **301** 1513
[3] International School of Physics Enrico Fermi, Inguscio M, Stringari S and Wieman C E, et Societa italiana di fisica 1998, 1999 Bose-Einstein condensation in atomic gases : Varenna on Lake Como, Villa Monastero, 7–17 July 1998, 1999.
[4] Ammann H and Christensen N 1997 Delta Kick cooling: a new method for cooling atoms *Phys. Rev. Lett.* **78** 2088–91
[5] Barrett B *et al* 2016 Dual matter-wave inertial sensors in weightlessness *Nat. Commun.* **7** 13786
[6] Graham P W, Hogan J M, Kasevich M A and Rajendran S 2013 New method for gravitational wave detection with atomic sensors *Phys. Rev. Lett.* **110** 171102
[7] Lounis B, Reichel J and Salomon C 1993 C. R. Acad. *Sci.* **316** 739
[8] Laurent P *et al* 1998 A cold atom clock in absence of gravity *Eur. Phys. J. - At. Mol. Opt. Plasma Phys.* **3** 201–4
[9] Nyman R A *et al* 2006 I.C.E.: a transportable atomic inertial sensor for test in microgravity *Appl. Phys.* B **84** 673–81
[10] van Zoest T *et al* 2010 Bose–Einstein condensation in microgravity *Science* **328** 1540
[11] Becker D *et al* 2018 Space-borne Bose–Einstein condensation for precision interferometry *Nature* **562** 391–5
[12] NASA web site, Cold Atom Laboratory on the ISS, private communication
[13] Liu L *et al* 2018 In-orbit operation of an atomic clock based on laser-cooled 87Rb atoms *Nat. Commun.* **9** 2760
[14] Petit G, Kanj A, Loyer S, Delporte J, Mercier F and Perosanz F 2015 1 × 10-16frequency transfer by GPS PPP with integer ambiguity resolution *Metrologia* **52** 301–9

[15] Salomon C *et al* 2001 Cold atoms in space and atomic clocks: ACES *Comptes Rendus Académie Sci. - Ser. IV – Phys.* **2** 1313–30

[16] Cacciapuoti L and Salomon C 2009 Space clocks and fundamental tests: the ACES experiment *Eur. Phys. J. Spec. Top.* **172** 57–68

[17] Laurent P, Massonnet D, Cacciapuoti L and Salomon C 2015 The ACES/PHARAO space mission *Meas. Time Mes. Temps* **16** 540–52

[18] Vessot R F C *et al* 1980 Test of relativistic gravitation with a space-borne hydrogen maser *Phys. Rev. Lett.* **45** 2081–4

[19] Delva P *et al* 2018 Gravitational redshift test using eccentric Galileo satellites *Phys. Rev. Lett.* **121** 231101

[20] Herrmann S *et al* 2018 Test of the gravitational redshift with Galileo satellites in an eccentric orbit *Phys. Rev. Lett.* **121** 231102

[21] Predehl K *et al* 2012 A 920-kilometer optical fiber link for frequency metrology at the 19th decimal place *Science* **336** 441

[22] Lopez O *et al* 2013 Simultaneous remote transfer of accurate timing and optical frequency over a public fiber network *Appl. Phys.* B **110** 3–6

[23] Chu S, Hollberg L, Bjorkholm J E, Cable A and Ashkin A 1985 Three-dimensional viscous confinement and cooling of atoms by resonance radiation pressure *Phys. Rev. Lett.* **55** 48–51

[24] Lévèque T *et al* 2015 PHARAO laser source flight model: design and performances *Rev. Sci. Instrum.* **86** 033104

[25] Peterman P, Gibble K, Laurent P and Salomon C 2016 Microwave lensing frequency shift of the PHARAO laser-cooled microgravity atomic clock *Metrologia* **53** 899–907

[26] Morić I, De Graeve C-M, Grosjean O and Laurent P 2014 Hysteresis prediction inside magnetic shields and application *Rev. Sci. Instrum.* **85** 075117

[27] Moric I *et al* 2014 Magnetic shielding of the cold atom space clock PHARAO *Acta. Astronaut.* **102** 287–94

[28] Guena J *et al* 2012 Progress in atomic fountains at LNE-SYRTE *IEEE Trans. Ultrason. Ferroelectr. Freq. Control* **59** 391–409

[29] Grop S *et al* 2011 ULISS: aMobile cryogenic ultra-stable oscillator, *2011 Joint Conf. of the IEEE Int. Frequency Control and the European Frequency and Time Forum (FCS) Proc.*, 2011, pp 1–4

[30] Laurent P *et al* 2006 Design of the cold atom PHARAO space clock and initial test results *Appl. Phys.* B **84** 683–90

[31] Laurent P *et al* 2014 PHARAO : the first primary frequency standard using cold atoms for space applications *Revue Française De Métrologie* **34** 2014–2

[32] Li R and Gibble K 2004 Phase variations in microwave cavities for atomic clocks *Metrologia* **41** 376–86

[33] Li R and Gibble K 2010 Evaluating and minimizing distributed cavity phase errors in atomic clocks *Metrologia* **47** 534–51

[34] Santarelli G, Audoin C, Makdissi A, Laurent P, Dick G J and Clairon A 1998 Frequency stability degradation of an oscillator slaved to a periodically interrogated atomic resonator *IEEE Trans. Ultrason. Ferroelectr. Freq. Control* **45** 887–94

[35] Santarelli G *et al* 1999 Quantum projection noise in an atomic fountain: a high stability cesium frequency standard *Phys. Rev. Lett.* **82** 4619–22

[36] Angstmann E J, Dzuba V A and Flambaum V V 2006 Frequency shift of hyperfine transitions due to blackbody radiation *Phys. Rev.* A **74** 023405

[37] Beloy K, Safronova U I and Derevianko A High-accuracy calculation of the blackbody radiation shift in the CS133 primary frequency standard *Phys. Rev. Lett.* **97** 4 040801 2006

[38] Gibble K and Chu S 1993 Laser-cooled Cs frequency standard and a measurement of the frequency shift due to ultracold collisions *Phys. Rev. Lett.* **70** 1771–4

[39] Berninger M *et al* 2013 Feshbach resonances, weakly bound molecular states, and coupled-channel potentials for cesium at high magnetic fields *Phys. Rev.* A **87** 032517

[40] Private communication Kokkelmans S and Hutson J M

[41] Gibble K 2012 Fountain clock accuracy, in 2012 European Frequency and Time Forum 16–18

[42] Guéna J, Li R, Gibble K, Bize S and Clairon A 2011 Evaluation of Doppler shifts to improve the accuracy of primary atomic fountain clocks *Phys. Rev. Lett.* **106** 130801

[43] Li R, Gibble K and Szymaniec K 2011 Improved accuracy of the NPL-CsF2 primary frequency standard: evaluation of distributed cavity phase and microwave lensing frequency shifts *Metrologia* **48** 283–9

[44] Weyers S, Gerginov V, Nemitz N, Li R and Gibble K 2011 Distributed cavity phase frequency shifts of the caesium fountain PTB-CSF2 *Metrologia* **49** 82–7

[45] Heavner T P *et al* 2014 First accuracy evaluation of NIST-F2 *Metrologia* **51** 174–82

[46] Gibble K 2015 Comment on 'First accuracy evaluation of NIST-F2′ *Metrologia* **52** 163–6

[47] Gibble K 2014 Ramsey spectroscopy, matter-wave interferometry, and the microwave-lensing frequency shift *Phys. Rev.* A **90** 015601

[48] Gibble K 2013 Scattering of cold-atom coherences by hot atoms: frequency shifts from background-gas collisions *Phys. Rev. Lett.* **110** 180802

[49] Szymaniec K, Lea S N and Liu K 2014 An evaluation of the frequency shift caused by collisions with background gas in the primary frequency standard NPL-CsF2 *IEEE Trans. Ultrason. Ferroelectr. Freq. Control* **61** 203–6

[50] Gerginov V, Nemitz N and Weyers S 2014 Initial atomic coherences and Ramsey frequency pulling in fountain clocks *Phys. Rev.* A **90** 033829

[51] Bize S, Sortais Y, Mandache C, Clairon A and Salomon C 2001 Cavity frequency pulling in cold atom fountains *IEEE Trans. Instrum. Meas.* **50** 503–6

[52] Fertig C and Gibble K 2000 Measurement and cancellation of the cold collision frequency shift in an Rb87 fountain clock *Phys. Rev. Lett.* **85** 1622–5